Detection and separation of x-rays, neutrons and charged particles using hybrid pixel detectors

Nachweis und Unterscheidung von Röntgenphotonen, Neutronen und geladenen Teilchen mit Hybriden Pixeldetektoren

Der Naturwissenschaftlichen Fakultät

der Friedrich-Alexander-Universität Erlangen-Nürnberg

zur

Erlangung des Doktorgrades Dr. rer. nat.

vorgelegt von

Benedikt Bergmann

aus Kronach

Als Dissertation genehmigt von der Naturwissenschaftlichen Fakultät
der Friedrich-Alexander-Universität Erlangen-Nürnberg

Tag der mündlichen Prüfung: 08.10.2019

Contents

1 | Introduction

1.1 Brief review of the history detectors for ionizing radiation

The detection of ionizing radiation has become increasingly important in fundamental research, medical applications, material analysis, dosimetry and many other fields. The fact that ionizing radiation covers a broad range of particle species and energies makes the development of radiation detectors challenging.
Radiation detection systems can be put to the following categories [Dem17]:

- Pure counting detectors, which solely register the amount of radiation quanta interaction without giving information about particle type or energy deposition;

- Track detectors, which "visualize" the trace or trajectory of a particle within the sensitive material;

- Spectroscopic devices, which measure the energy deposition of ionizing radiation in the sensitive volume;

- A combination of the above.

The earliest discoveries in the field of ionizing radiation were made around the turn of the 20th century using phosphorous plates and photographic emulsions. While these radiation sensitive devices were integrating devices, Rutherford and Geiger [RG08] later proposed a gas-filled radiation detector. This laid the basis for detectors counting individual quanta of ionizing radiation. The Geiger-Müller tube [GM28], developed in 1928, is a pure counting device and still extensively used even today. Its main drawback is that it is not sensitive to particle type or deposited energy. Other examples of historically significant radiation detector technologies are cloud [Wil11] and bubble chambers [Gla52], in which ionizing radiation is visualized in the form of tracks. The cloud chamber measurement that led to the discovery of the positron in 1932 [And33] is shown in Fig.1.1.

Further development in the area of radiation detection resulted in more sophisticated detection systems. One of the most notable recent steps in the process of this development was the invention of the multi-wire proportional chamber [CBB$^+$68], which was awarded the Nobel Prize in 1992. Today, due to application-specific demands with respect to precision, sizes and cost, detection systems have become increasingly specialized.

Detector technology used in the work presented is the semiconductor hybrid pixel detector. The practical use of semiconductor detectors started in the 1960s, when the semiconductor industry was first established, allowing easier access to silicon or germanium detectors. In the beginning, such detectors were referred to as "crystal counters", highlighting the analogy to gaseous counting devices [Owe12]. Nowadays, the term solid-state or semiconductor detectors is more common. Compared to gaseous detectors, solid state devices have several advantages [Dem17]:
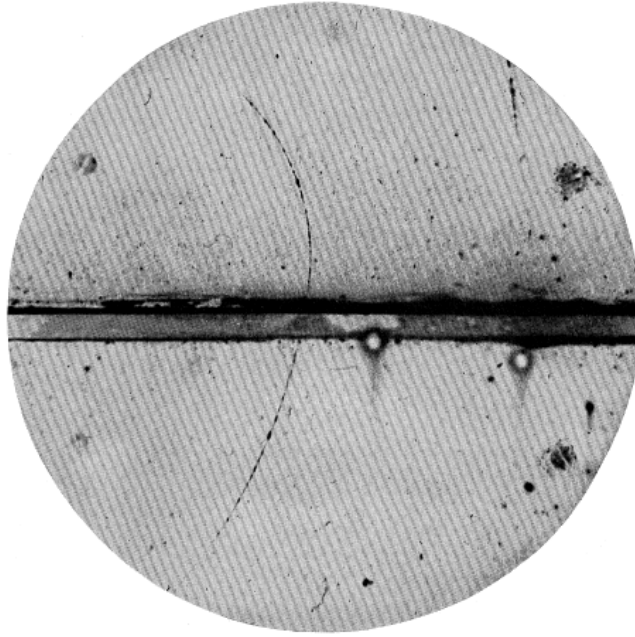
Figure 1.1: One of the images of the cloud chamber measurement which led to the discovery of the positron. By evaluating the curvature and lengths of the track before and after a 6 mm thick lead plate it could be demonstrated that the registered particle was positively charged and lighter than a proton. From: [And33]

- The density of a semiconductor is higher by several orders of magnitude than that of gases. This results in smaller volumes, which are needed to slow down energetic particles. Consequently, compact devices can be produced. Another useful side effect of small devices is that charge collection times are in the order of 10 - 100 ns and thus significantly faster than in gas detectors;

- Due to the lower energy needed for the creation of free carriers, their number per unit energy loss is higher. This gives a higher dynamic range (lower value of the minimal energy deposition in order to be seen) and better spectroscopic performance. In this respect, semiconductor devices also outperform scintillation detectors.

The semiconductor material currently dominating the market is silicon. However, when it comes to precise x- or γ-ray spectroscopy, germanium is still the material of choice.

1.2 Hybrid pixel detectors

Semiconductor hybrid pixel detectors are the foundation of the applications and experiments discussed in the presented work. Originally, the development of hybrid pixel detectors focused towards the needs of particle tracking in the inner vertex detectors of the Large Hadron Collider (LHC). In 1997, the Medipix collaboration was formed to exploit the capabilities of such detection systems in biomedical applications [BCL17]. The outputs of the Medipix collaborations were pure photon counting devices (Medipix, Medipix2, and Medipix3), and also devices where the collected charge and/or time of interaction is recorded in each pixel (Timepix and Timepix3). These detectors have found applications in x-ray and neutron imaging [Jak09], particle therapy [MJG$^+$11, JGH$^+$11], Brachytherapy [PLSN$^+$13, LJZ$^+$14]), material science [Jak09], and in Space, where they

2

are used for radiation monitoring and dosimetry on the ISS [TPJ[+]11a] or the measurement of the fluxes and the directions of trapped particles in the Van-Allen radiation belts [GBG[+]16]).

1.3 Outline of the thesis

The aim of this thesis was to carry out experiments for nuclear, atomic and particle physics which profit from the new technology of time- and position resolving pixel detectors of the Timepix family. Different detection setups were designed to increase particle-type dependent sensitivities for x-ray, neutron and charged particle detection. Therefore, the response of the pixel detectors to different types of radiation was investigated in simulation and experiments. The key features exploited were the time resolution, which allowed coincidence (and anticoincidence) measurements and doing a 3D reconstruction of particle trajectories (for the Timepix3), and the spatial resolution, which was used for the determination of the angular distribution of an x-ray signal and for basic particle species determination and separation using pattern recognition.

The introduction is followed by 6 chapters:

- Chapter 2 is an introductory chapter to the Medipix/Timepix detector family. It gives details about chip developments in the Medipix collaborations and discusses the Timepix's and Timepix3's working principles;

- Chapter 3 reviews the principles of interactions of radiation with matter and demonstrates the characteristic imprints left by different ionizing particles in the sensor layer of a Timepix detector;

- Chapter 4 discusses the application of a stack consisting of two Timepix detectors in a coincidence experiment to measure the double vacancy production probability in the electron capture decay of ^{55}Fe. This is the first time, pixelated detectors have been used for such an investigation. Therefore, a first measurement of the angular correlation function between the hypersatellite and satellite photon is presented;

- Chapter 5 addresses the development of an active neutron detector, which was designed in particular for remote use in the ATLAS detector at CERN[1], but could be used in any mixed radiation field. Neutron calibration methods are explained and typical data evaluation in different mixed radiation fields (in particle therapy, at a neutron beam line, and at different sites within the ATLAS experiment) are outlined;

- Chapter 6 describes a measurement with Timepix3 in a fast neutron beam to increase the knowledge of fast neutron interactions in silicon, as the most common detector material, and to study the competition of ionizing and non-ionizing energy losses of recoil silicon atoms in a silicon lattice. The importance of the results is discussed in the context of radiation damage (to the sensor material);

- Chapter 7 evaluates Timepix3 performance in the application of particle trajectory reconstruction (particle tracking). Hereby, the improved time resolution is used to determine the z-coordinate and perform 3D reconstructions of particle trajectories within the sensor volume.

---

[1]Conseil europeen pour la recherche nucleaire

2 | The Medipix/Timepix detector family

2.1 Basic facts

Medipix/Timepix detectors are hybrid pixel detectors, developed within the Medipix collaboration founded by CERN [MPX]. The Medipix collaboration's aim was to bring technology developed for particle tracking at the LHC to biomedical applications. The first chip, which was fabricated in 1997, was a pure photon counting chip called Medipix. It was segmented into 64×64 pixels, with a pixel pitch of $170\,\mu$m. Research and development then continued in two directions:

- Improvement of photon counting chips. This led to the development of Medipix2 and Medipix3 with smaller pixels and additional features such as additional discrimination thresholds and the charge summing mode (CSM);

- Development of chips extracting information about the time of interaction (time-of-arrival, ToA) or/and the charge deposit in each pixel (time-over-threshold, ToT). This led to the development of the first Timepix [LBCT07] and later on the Timepix3 [PPW$^+$14].

An overview of detectors currently available is given in Table 2.1. A comprehensive review of chip designs and their applications can be found in [BCL17]. Small, compact, and easy to use readout systems, such as the USB readout for MPX2 [PBJ$^+$08], the FITPix interface [KHJ$^+$11], miniaturized versions (like the USB Lite or the FITPix Lite), and the corresponding software package Pixelman [THJ$^+$11] were developed for detector control.

	Medipix	Medipix2	Timepix	Medipix3	Timepix3
Pixel pitch [μm]	170	55	55	55 / 110	55
No. of pixels in x and y	64	256	256	256 / 128	256
Technology [nm]	1000	250	250	130	130
Front end noise [e$^-$ RMS]	170	110	100	80 in SPM[1] 174 in CSM[2]	62
ToT/ToA	-	-	ToT **OR** ToA	-	ToT **AND** ToA
Time (ToA) resolution [ns]	-	-	up to 10	-	1.5625

[1] Single Pixel Mode
[2] Charge Summing Mode

Table 2.1: Overview of the existing ASICs developed by the Medipix Collaborations.
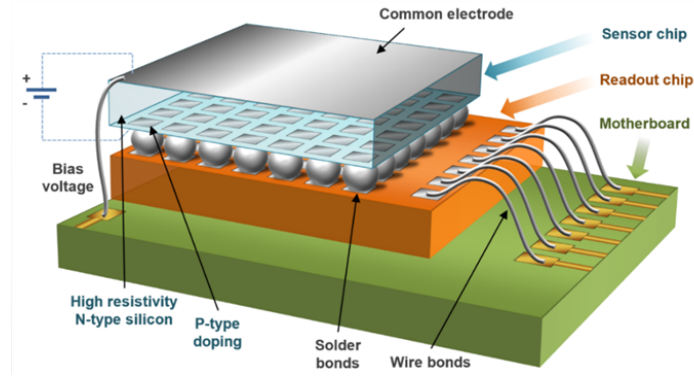
Figure 2.1: Illustration of a Medipix/Timepix assembly.

2.2 Working principles

The basic concept of a hybrid pixel detector is the separation of the detection medium (typically called the sensor layer) from the readout electronics, so that - depending on the application - different sensor layers can be used on the same chip. Typical sensor materials are room temperature semiconductors such as silicon, GaAs, CdTe, or CdZnTe. Figure 2.1 illustrates schematically the basic structure of a Medipix/Timepix assembly. Each pixel of the sensor layer is connected to the readout chip (ASIC) through so-called solder bumps (or bump-bonds) [BCL07].

By reverse biasing the sensor layer a fully depleted volume is created, in which ionizing radiation interaction creates free charge carriers (electrons e$^-$ and holes h$^+$), whose average number is proportional to the energy deposition in the volume: $N = \frac{E_{dep}}{\omega}$, where ω is the ionization energy, the average energy transfer needed to elevate an electron from the valence band to the conduction band by an ionizing particle, of the medium (for example 3.36 keV for silicon). The process of creating free charge carriers is not purely statistical in nature. As a result, fluctuations σ in the number of created charge carriers differ from the $\sqrt{N}$ as expected from a poissonian distribution. This is described by $\sigma = \sqrt{FN}$ [Fan47, Dur08], with the Fano factor F.

The created free charge carriers drift through the sensor layer due to an applied potential difference between the back-side and the pixelated contact. Depending on the sensor material and contact scheme, either holes or electrons are collected at the pixelated side. The drift velocity $\vec{v}_{e,h}$ of the charge carriers is directly proportional to the electric field $\vec{E}$ up to a critical electric field strength of $E_{max} \approx 3\,\text{kV}\,\text{cm}^{-1}$ [Owe12]. This relation is given by:

$$\vec{v}_e = \quad - \quad \mu_e \vec{E} \tag{2.1}$$
$$\vec{v}_h = \qquad \mu_h \vec{E}, \tag{2.2}$$

whereby the proportional constant is called the mobility $\mu_{e,h}$. For field strength higher than E_{max}, the drift velocity reaches a saturation level.

A lateral component to the charge carrier motion is caused by diffusion and repulsion, which results in a broadening of the initial charge cloud. The diffusion width is described by:

$$\sigma(t) = \sqrt{2Dt} = \sqrt{\frac{2k_B T \mu_{e,h} t}{q}} \tag{2.3}$$

where t is the drift time, D the diffusion constant, k_B the Boltzmann constant, T the temperature and q the charge [SH85]. A model for the repulsion was presented by [GLRS87] and [Kor07], who

calculated the broadening of a cylindrical and spherical charge cloud in the initial state. For the cylindrical charge cloud the broadening due to repulsion $r(t)$ can be approximated by

$$r_{\text{cyl.}}(t) = \sqrt{\frac{\mu_{\text{e,h}}}{\pi \epsilon_r \epsilon_0} \rho t}, \tag{2.4}$$

with ρ the charge density per area in a cylindrical volume, ϵ_0 the electric constant and ϵ_r the relative permittivity. For the spherical charge cloud, the expansion due to repulsion is described by

$$r_{\text{spher.}}(t) = \sqrt[3]{3 \frac{\mu_{\text{e,h}} q}{4 \pi \epsilon \epsilon_0} N t}, \tag{2.5}$$

where N denotes the number of charge carriers. As a result, an initially small charge cloud can be spread over an area of connected pixels, forming a so-called cluster. Each pixel within the cluster contributes its part to the total energy deposition so that by summing the energies in each pixel, the initial charge deposition can be recalculated. The distribution of charge to neighboring pixels is called charge sharing.

During drift and collection, the charge carriers induce currents at the pixel electrodes nearest to their positions [Sho38, Ram39]. These are converted to voltage pulses in the analogue part of the pixel electronics and subsequently amplified. Figure 2.2 schematically illustrates the voltage pulse after the charge sensitive preamplifier. This pulse is compared to a globally adjustable threshold level (THL) and - depending on the mode of operation and chip type - the information about number of interactions, amount of collected charges and/or time of interaction is obtained. The modes of operation are discussed for Timepix and Timepix3 in the following.

2.3   Timepix

The Timepix detector is a modified version of the Medipix2 with 65,536 (256×256) pixels at a pixel pitch of $55\,\mu$m. It is designed using 250 nm CMOS technology. Timepix fully relies on a frame-based readout scheme, which is a concept similar to a commercial photographic camera, whereby the acquisition is started and stopped by opening and closing a shutter. Once the shutter is opened, the pixel matrix becomes active. After the shutter is closed the status of each pixel is read out and the detector is not capable of registering further events. The latency caused due to this process is about 11 ms. The 2D "image" showing the status of each pixel after the given acquisition time is called frame.

The Timepix pixels can be set to one of three modes, illustrated in Fig. 2.2:

1. Counting (or Medipix) mode, where the pixel counter is incremented once the voltage output pulse crosses the THL level;

2. Time-of-Arrival (ToA) mode, where the time is sampled with a clock from the crossing of the THL level until the time of the shutter closing;

3. Time-over-Threshold (ToT) mode, where the time interval the pulse stays above the THL is measured. By calibration with characteristic x-ray fluorescence lines [Jak11] the lengths of the pulses can be related to energy deposit.

Each pixel is equipped with a 14-bit pseudo-random counter (counter depth: 11,810) to store the registered values.
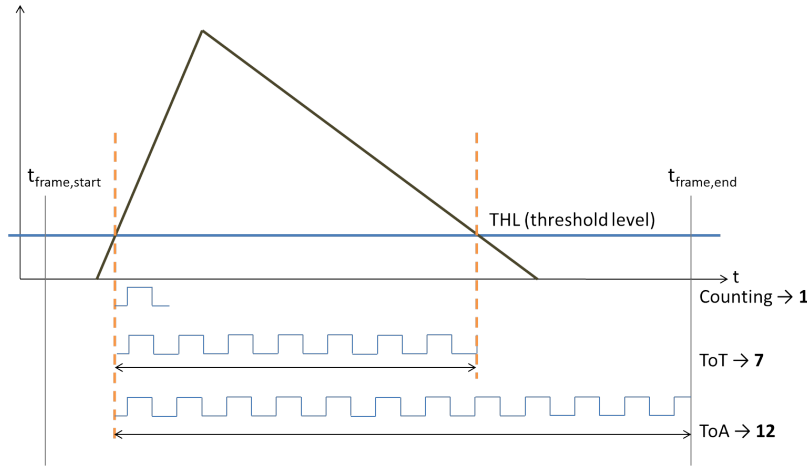
Figure 2.2: Illustration of the 3 modes of operation of a Timepix detector. The Timepix pixel can be set to counting, ToT or ToA mode.

The maximal clock frequency, which can be used for ToT and ToA measurements is 48 MHz (time resolution: 20.8 ns) with the FITPix [KHJ$^+$11] and 96 MHz (10.4 ns time resolution) with the MUROS2 readout [BvBJ$^+$03]. In typical conditions, noise-free operation can be achieved at a THL of $\approx 1000\,\mathrm{e}^-$ (corresponding to 3.6 keV in silicon).

Depending on particle type, interaction depth and sensor thickness, a single particle can be seen in a single pixel or cover an area of neighboring pixels (see the discussion in Chapter 3). The created conglomeration of neighboring pixels is called cluster or track.

The main consequence of the frame-based readout scheme is that a frame time adjustment is needed to guarantee proper results. Depending on the mode of operation different aspects have to be considered:

- In counting mode, the frame times have to be short enough to not trigger the pixel more often than the counter depth.

- In ToT mode, the frame time has to be set short enough to avoid significant track overlapping, keeping in mind that too short frames increase the probability of cutting the pulse on its downward slope, thus corrupting the ToT information. Desirable are pixelmatrix occupancies of 15 % or below.

- In ToA mode, the frame lengths have to be set in such a way so that the timestamps of pixels registering hits at the beginning of the frame do not exceed the counter depth. This means, that for a given clock frequency, the maximal possible frame acquisition time is given by $t_{\mathrm{acq.}} = 11,810/f_{\mathrm{clock}}$.

2.4   Timepix3

The latest generation of the Medipix/Timepix family is the Timepix3 chip, which is designed in 130 nm technology. It features a data-driven readout scheme and allows simultaneous measurement of ToA (18 bit) and ToT (10 bit). In a data-driven readout, only the pixel which has seen an event is read out, while all other pixels stay active. A triggered pixels is not capable of detecting another event for approximately 475 ns.
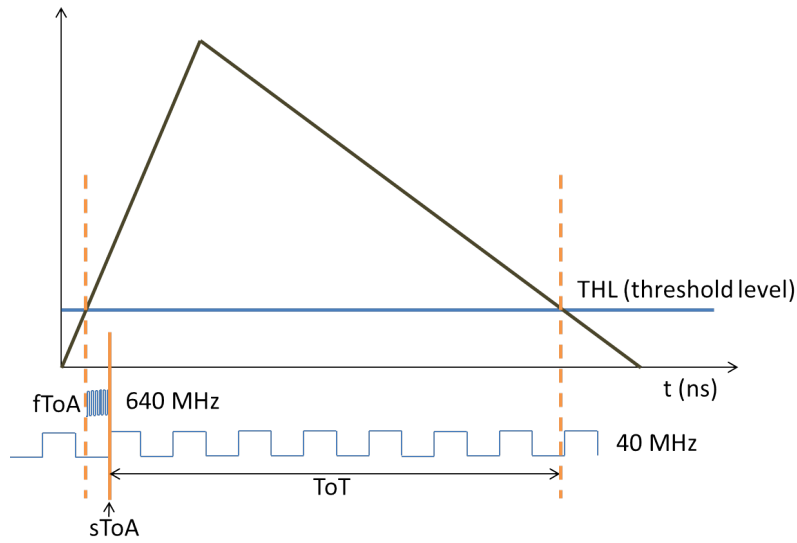
Figure 2.3: Illustration of working principles of a Timepix3. The Timepix3 measures the ToA and ToT simultaneously in each pixel. To improve the time resolution a 640 MHz clock determines the time from the crossing of the THL until the next rising edge of the base 40 MHz clock.

A 40 MHz base clock is continuously running and used to determine the ToT and the sToA (slow ToA). With an additional 640 MHz clock from a ring oscillator (fToA) sampling the time from the actual crossing of the THL until the next rising edge of the sToA, a time resolution of 1.5625 ns can be achieved (see Fig. 2.3). The final time stamp is given by $t[\mathrm{ns}] = \mathrm{sToA} \times 25 - \mathrm{fToA} \times 1.5625$. In contrast to Timepix, where time is measured with respect to the end of the frame, the time is determined relative to the beginning of the data acquisition. Due to the improved time resolution, the time-walk effect becomes visible. Time-walk means that pulses starting at the same time but with lower amplitudes are assigned to a later time-stamp, when compared with pulses of greater amplitude. It can be corrected for by using the external test pulses utility [FCG+15] or by using the experimental approach described in [TJS16] and in Chapter 7 of this thesis. The advantage of the latter is that it uses pulse shapes, which include charge transport and induction effects.

Noise free operation with a Timepix3 chip should be possible at a THL of $\approx 500\,\mathrm{e}^-$ (1.8 keV in silicon). However, due to the high power consumption of the chip, this can only be achieved with proper cooling. Sophisticated readout systems for the Timepix3, such as the Spidr [vdHVvB+17], AdvaDAQ [TJS16] and the Kathrine [BBJ+17], have recently become available.

3 | Radiation detection with the Timepix detector

As described in Sec. 2, the detection of ionizing radiation in a semiconductor device is associated with the measurement of charge carriers created in the sensor material. Depending on particle type and energy, the ionization is caused by different processes, which are briefly addressed in the following.

3.1 Charged particles

The energy losses of charged particles along their trajectory through a medium are mostly due to single elastic collisions with the atomic electrons. In each of these collisions an energy W is transferred. The theoretical description of this process was started by Bohr [Boh87] and treated quantum mechanically by Bethe [Bet30], Bloch [Blo33] and Landau [Lan44].

For intermediate energies ($0.1 < \beta\gamma < 1000$) and intermediate Z-materials the Bethe-Bloch formula reads as [O$^+$14]:

$$\left\langle -\frac{dE}{dx} \right\rangle = Kz^2 \frac{Z}{A} \frac{1}{\beta^2} \left[\frac{1}{2} \ln \frac{2m_\mathrm{e}c^2 \beta^2 \gamma^2 W_\mathrm{max}}{I^2} - \beta^2 - \frac{\delta(\beta\gamma)}{2} \right]. \tag{3.1}$$

Here, z denotes the projectile's charge, $K = 4\pi N_\mathrm{A} r_e^2 m_e c^2 = 0.307\,\mathrm{MeV\ mol^{-1}\ cm^{-2}}$, I the mean excitation energy of the material, Z the atomic number of the absorber, and A its mass number. $\beta = v/c$ is the ratio of the particle velocity to the speed of light. $\gamma = \sqrt{1-\beta^2}^{-1}$ is the Lorentzfactor. $\delta(\beta\gamma)$ is a density effect correction to the ionizing energy loss.

With increasing particle energy the stopping power reaches a maximum, then goes through a broad minimum and increases again. Particles close to the minimum of their stopping power curve are referred to as minimum ionizing particles (mips). W_max is the maximum energy transfer in a single collision and given by [O$^+$14]:

$$W_\mathrm{max} = \frac{2m_\mathrm{e}c^2\beta^2\gamma^2}{1 + 2\gamma m_\mathrm{e}/M + (m_\mathrm{e}/M)^2}, \tag{3.2}$$

where M is the incident particle mass. Even though in most of the collisions the energy transfer to the electron is low, the maximum energy transfer can be relatively high giving rise to electrons traveling away from the initial ion trajectory. Such electrons are referred to as "δ-rays". They are a key feature of relativistic ion tracks in the Timepix detectors. Measured tracks with outgoing δ-rays are shown in Figs. 3.1 (Timepix) and 3.2 (Timepix3). They consist of:

- A "core" region describing the trajectory of the initial ion, which is broadened due to the charge sharing;

- A "halo" of pixel measuring low energies (typically below 10 keV). The current understanding is that this feature is a combination of the per-pixel processing scheme and charge induction: Induced current pulses next to charge collecting pixels exhibit a bipolar signal with equal areas below the curves in either polarity [Kre06]. Thus, in such pixel in an integrating device, positive and negative signal would cancel each other out. In Timepix however, either the positive or the negative part of the pulse is measured, so that a pixel hit is registered if the induced charge with proper polarity goes above the threshold [JT]. The extent of the halo depends on interaction depth, pulse shaping, sampling speed, energy deposition and detector settings (mainly threshold and bias voltage);

- Outgoing δ-rays.

Further discussion can be found, for example in [PEG$^+$11, HVP$^+$14]. The density of δ-rays along the particle trajectory with kinetic energies $T >> I$ is given by [O$^+$14]:

$$\frac{d^2 N}{dx\, dT} = \frac{1}{2} K z^2 \frac{Z}{A} \frac{1}{\beta^2} \frac{F(T)}{T^2},$$ (3.3)

with a spin-dependent factor $F(T)$. Analytical expressions of $F(T)$ are given in [O$^+$14] for spin-0, and in [Ros52] for spin 1/2 and spin 1 particles . The δ-ray (kinetic energy T_e, momentum p_e) is ejected at the angle [O$^+$14]:

$$\theta = \cos^{-1}\left(T_e/W_{\max} \frac{p_{\max}}{p_e} \right),$$ (3.4)

with respect to the momentum of the ionizing particle, where $p_{\max}$ is the momentum of an electron with energy $W_{\max}$.

The fluctuation of a particle's energy loss in a medium of thickness x follows a Landau distribution. The most probable energy loss is given by [Bic88]:

$$\Delta_p = \zeta \left[\ln \frac{2 m_e c^2 \beta^2 \gamma^2}{I} + \ln \frac{\zeta}{I} + j - \beta^2 - \delta(\beta\gamma) \right],$$ (3.5)
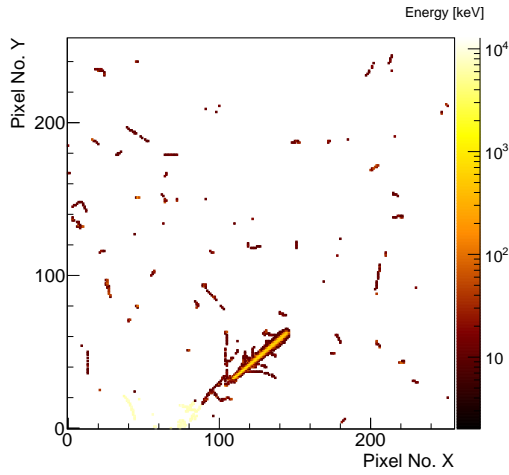
where $j = 0.200$ [Bic88] and ζ [MeV] $= (K/2)\langle Z/A \rangle (x/\beta^2)$. As an example, the ionizing energy losses of a 40 GeV/c pion on its path through a 500 μm thick silicon sensor attached to a Timepix3 as measured in the SPS[1] at CERN are shown in Fig. 3.3. The distribution was fitted by a Landau distribution convoluted with a Gaussian, which accounts for the smearing due to the energy resolution. The most probable energy loss from the fit $\Delta_{p,fit} = 146.5$ keV can be compared with the one calculated according to Eq. (3.5): $\Delta_{p,calc.} = 145$ keV when considering the energy resolution, which was found to be $\sigma_E = 9.4$ keV.

From Eq. (3.1) the range R_{CSDA} of a particle in a medium may be approximated by integrating the reciprocal of the stopping power $R_{CSDA} = \int_E^0 (-dE/dx)^{-1}\, dE$, which is referred to as the continuous slowing down approximation (CSDA). Figure 3.4a shows the Timepix3 energy response to a proton of 1 MeV, which has a CSDA range of 16.5 μm[2] in silicon and to an α-particle of (5.5 MeV) (CSDA range: 27.8 μm[3]). Both particles deposit their energy in a small volume (less than one pixel) close to the sensor surface. However, due to the expansion of the created charge cloud as a result of diffusion and repulsion, extended clusters are created. It was shown in [JCH$^+$08], that subpixel spatial resolution (≈ 300 nm) can be achieved by modeling the cluster shape. For particles at the

---

[1]Super Proton Synchrotron

[2]Calculated with the PSTAR program: https://physics.nist.gov/PhysRefData/Star/Text/PSTAR.html

[3]Calculated with the ASTAR program: https://physics.nist.gov/PhysRefData/Star/Text/ASTAR.html

(a) A frame with an ion track measured with the Space Application of Timepix Radiation Monitor (SATRAM) [GPV+16], which is based on a Timepix with 300 μm thick silicon sensor layer, flying in low earth orbit (at an altitude of 820 km).
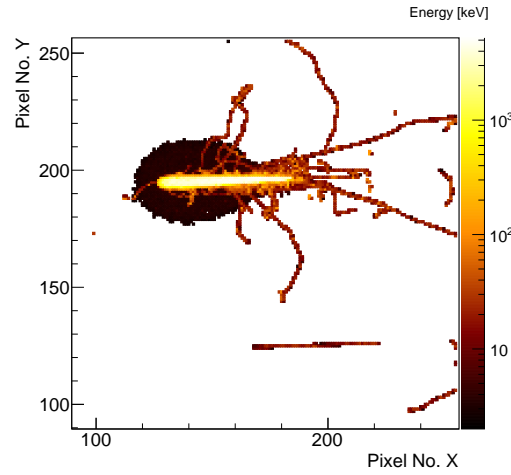
(b) 75 GeV/c argon ion track passing through a 1 mm thick sensor layer at an angle of 70°. The measurement was done at the SPS facility at CERN.
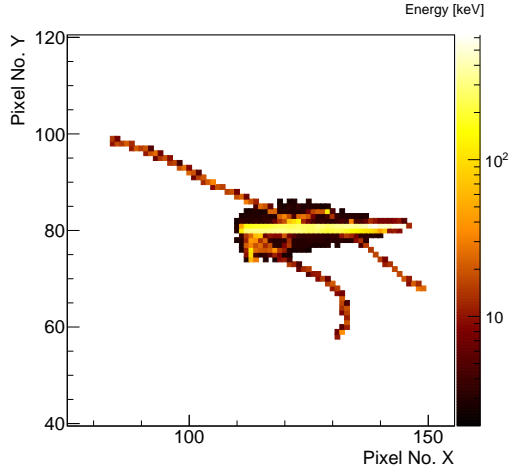
(c) 1 GeV/A carbon ion track passing through a 1 mm thick sensor layer at an angle of 60°. The measurement was done at the Joint Institute of Nuclear Research (JINR) in Dubna.
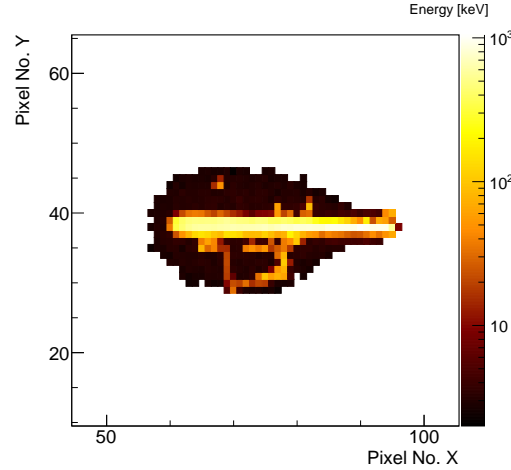
(d) 430 MeV/A carbon ion track passing through a 1 mm thick sensor layer at an angle of 60°. The measurement was done in the Heidelberg Ion Therapy center (HIT).

Figure 3.1: Examples of tracks with delta-rays measured with Timepix detectors.

13
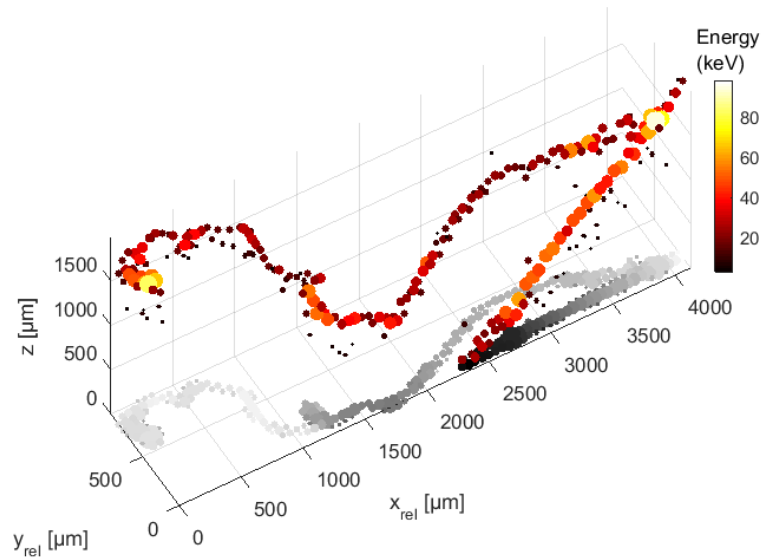
Figure 3.2: 40 GeV/c pion passing through a 2 mm thick CdTe sensor layer on a Timepix3 chip at 45°. The excellent time resolution of Timepix3 allows the reconstruction of the particle trajectory in 3D (details are described in Chapter 7). A δ-ray track is clearly visible.

Entries	1731435
χ^2 / ndf	6588 / 443
Width (keV)	9.548
Δ_p (keV)	146.5
Area	1.749e+006
σ_{Gauss} (keV)	9.9

Figure 3.3: Energy loss distribution of 40 GeV/c pions in a 500 μm thick silicon sensor (Timepix3 assembly, blue) with a model fit (red curve). The fluctuations of the ionizing energy depositions are described by a Landau distribution. This distribution is convoluted with a Gaussian to take into account the energy resolution of the detector. This measurement was done at the SPS at CERN.
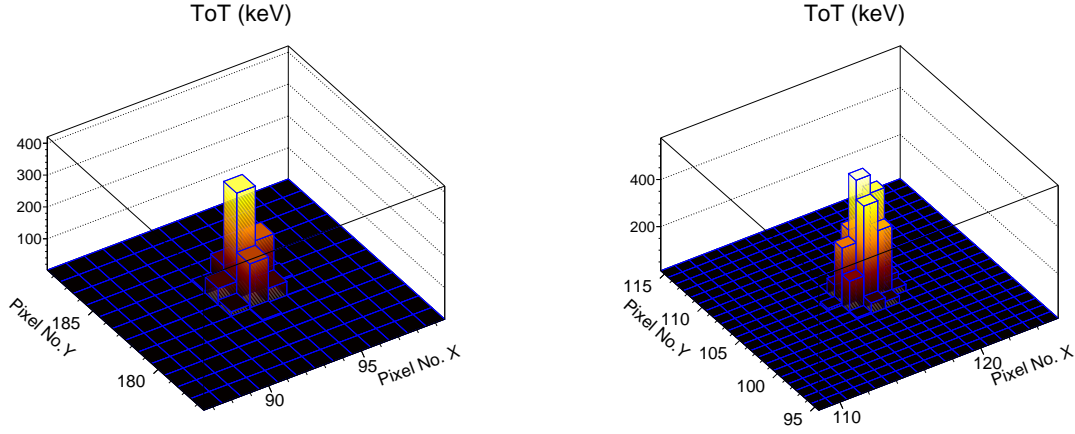
(a) 1 MeV proton (CSDA range: $16.5\,\mu$m) measured by a Timepix3 with a $500\,\mu$m thick silicon sensor layer.

(b) 5.5 MeV α-particle from an ^{241}Am source (CSDA range: $27.8\,\mu$m) measured by a Timepix3 with a $500\,\mu$m thick silicon sensor layer.

Figure 3.4: Timepix response to particles with low range.

end of their range, decreasing projectile energy is related to increase in the ionizing energy deposition, which results in the so-called "Bragg-peak" when a particle is completely absorbed in the medium. The Bragg peak of a 50 MeV/A helium ion absorbed in the silicon sensor of a Timepix is illustrated in Fig. 3.5. The Bragg-behavior of charged particles has found an application in particle therapy where it is used to deliver the maximal dose to the tumor region while reducing dose to healthy tissue.

At low energies, corrections to the Bethe-Bloch formula have to be considered to improve precision. These are the implementation of shell corrections by adding the term C/Z into the square brackets of Eq. (3.1) and higher order contributions like the "Bloch" ($z^2 L_2(\beta)$) and the "Barkas correction" ($z L_1(\beta)$). Collisions with the nuclei in the medium become important especially for heavier ions and at particle velocities less than 0.1 c [O$^+$14]. Such collisions lead to so-called non-ionizing energy losses, which are discussed in greater detail in Chapter 6.
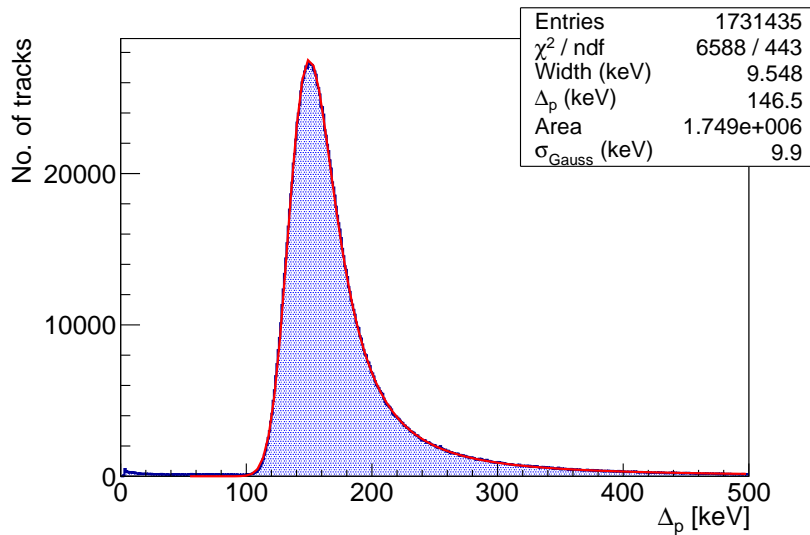
3.2 Electrons

Since electrons carry charge, they also lose their energy through collisions with the electrons in the sensor material. However, electrons are lighter than the above discussed ions, so that deflections at higher angles are more likely to occur. Therefore, electrons typically create jagged paths in the Timepix sensor layers. Examples of electron tracks are shown in Fig. 3.6, which depicts internal conversion electrons and photoelectrons (see Sec. 3.3) in a $500\,\mu$m thick silicon sensor layer of a Timepix3 when placed in the radiation field of a ^{54}Mn electron capture source.

Two loss mechanisms contribute to the energy losses of electrons: collisional losses $-(dE/dx)_{\mathrm{c}}$ and, since every deflection is associated with the acceleration of charge, radiative losses $-(dE/dx)_{\mathrm{r}}$. The collisional losses are described by [Kno89]:

$$-\left(\frac{dE}{dx}\right)_{\mathrm{c}} = \frac{2\pi e^4 N Z}{m_e v^2}\left[\ln\left(\frac{m_e v^2 E}{2 I^2 (1-\beta^2)}\right) + \ln(2)\left(2\sqrt{1-\beta^2} - 1 + \beta^2\right) + (1-\beta^2) + \frac{1}{8}\left(1 - \sqrt{1-\beta^2}\right)^2\right],$$
(3.6)
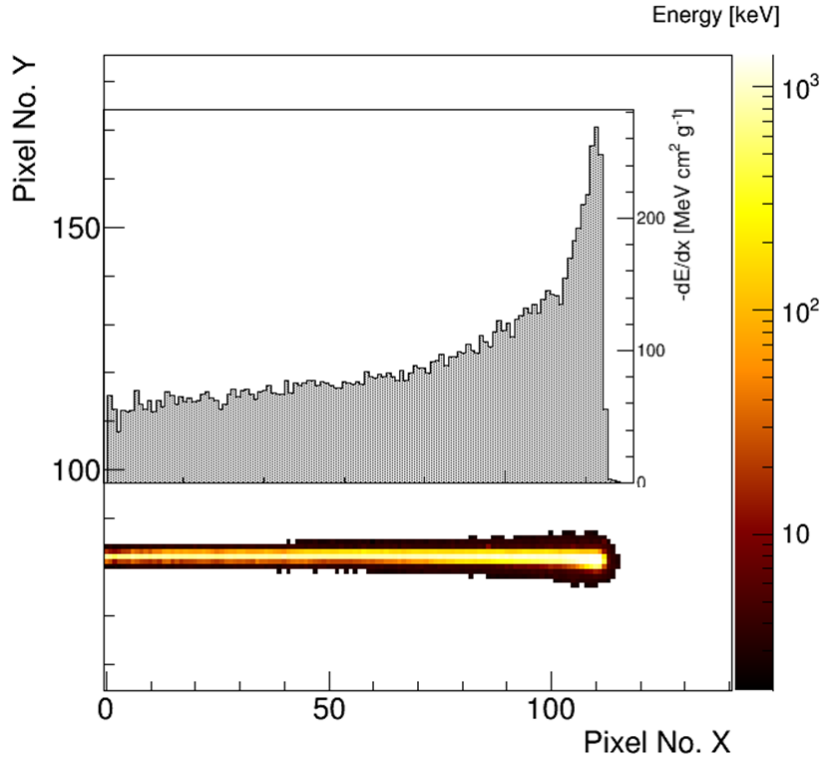
Figure 3.5: 50 MeV/A helium ion entering from the side into the Timepix detector. It is completely absorbed in the silicon sensor layer. The inlay illustrates the energy depositions along the particle trajectory. Energy deposition increases at the end of the particle trajectory resulting in the so-called "Bragg"-peak.

where N denotes the number density. The radiative losses are given by [Kno89]:

$$-\left(\frac{dE}{dx}\right)_{\text{r}} = \frac{NEZ(Z+1)e^4}{137 m_e^2 c^4}\left(4\ln\left(\frac{2E}{m_e c^2}\right) + \frac{4}{3}\right). \tag{3.7}$$

The total linear stopping power of electrons is thus determined by the sum of the collisional and radiative losses as:

$$\frac{dE}{dx} = \left(\frac{dE}{dx}\right)_{\text{c}} + \left(\frac{dE}{dx}\right)_{\text{r}}. \tag{3.8}$$

3.3 Photons

Photons deposit energy in a sensor material by the photoelectric effect, the Compton effect, and pair production. Thus, the neutral photons are converted to detectable electrons or an electron positron pair. This inherently means that the signature of photons and electrons in the detector are equal, if only the 2D projections are detectable. Figure 3.7 shows the energy ranges, for which the different processes dominate.

The photoelectric effect

The photoelectric effect involves complete energy transfer of the photon to the atomic shell. If the photon energy is bigger than the energy needed to elevate the electron to the continuum, an
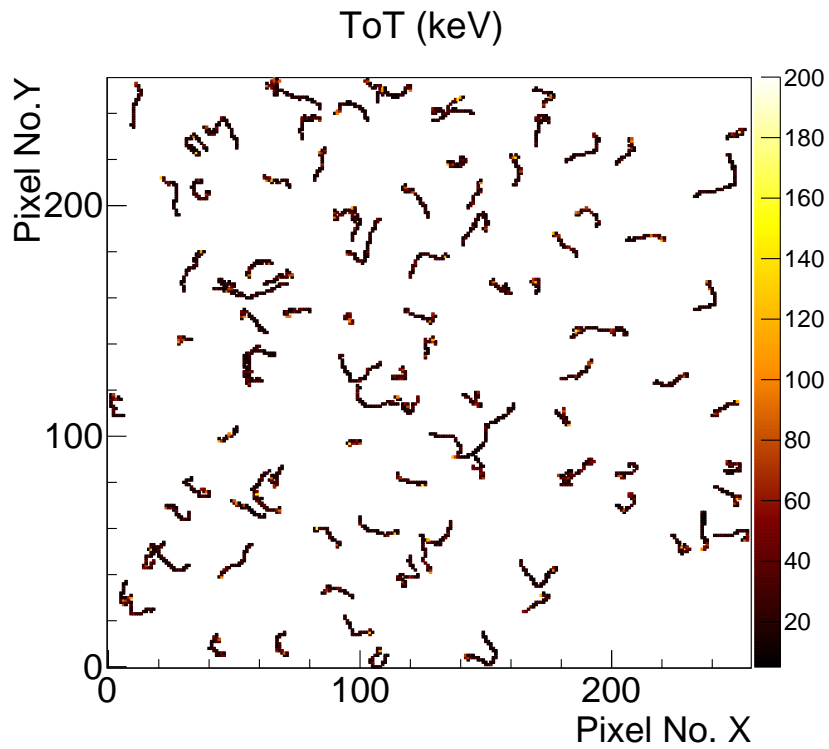
Figure 3.6: 835 keV electrons from internal conversion and electrons from the photoelectric effect in the silicon sensor after the electron capture decay of ^{54}Mn in a 500 μm thick silicon (Timepix3 assembly). Photons are converted to electrons in the sensor layer and thus they are seen with the same signature.
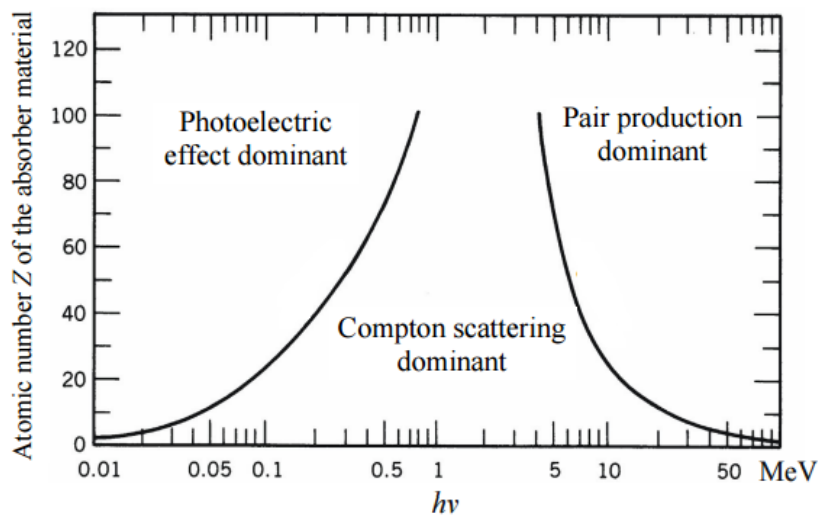
Figure 3.7: Regions of dominance of interaction processes between photons and matter. Lines separate the regions where the different photon interactions dominate [abs].

electron is released from the excited atomic shell. The energy of the released electron is given by $E = E_{\mathrm{photon}} - \Phi$, where Φ is a material-dependent constant (work function). It describes the energy needed to elevate the electron from a bound state to the continuum. The ionized atom in the final state relaxes through Auger electron or characteristic x-ray emission. Whereas Auger electron ranges are typically short, x-rays can have enough energy to leave the sensitive volume (or pixel) giving rise to a so-called escape peak in the recorded energy spectra. Photoelectric absorption is most efficient for low photon energies and high-Z materials. Its cross section decreases with $E^{-3.5}$ and increases with Z^5. Since the photo-electron has approximately the same energy as the incident photon, for monoenergetic photon impact this effect causes a peak in the energy spectrum.

The Compton effect

The Compton effect describes the scattering of a photon off a free electron. The energy of the incident photon is thus shared amongst the electron and the scattered photon, which can leave the sensitive volume again. The energy transfer to the electron depends on the scattering angle θ. It is given by:

$$E_e' = E_\gamma \times \frac{1}{1 + \frac{m_e c^2}{E_\gamma (1 - \cos(\theta))}}. \tag{3.9}$$

The total cross section $\sigma_{\mathrm{C}}^{\mathrm{KN}}$ of the Compton effect is described by the Klein-Nishina formula [KN29]:

$$\sigma_{\mathrm{C}}^{\mathrm{KN}} = 2\pi r_0^2 \left\{ \frac{1+\alpha}{\alpha^2} \left[\frac{2(1+\alpha)}{1+2\alpha} - \frac{\ln(1+2\alpha)}{2\alpha} \right] + \frac{\ln(1+2\alpha)}{2\alpha} - \frac{1+3\alpha}{(1+2\alpha)^2} \right\} [\mathrm{cm}^2 \mathrm{electron}^{-1}], \tag{3.10}$$

where $\alpha = \frac{E_e'}{m_e c^2}$ and r_0 the classical electron radius. It increases linearly with Z and decreases with E_γ.

In measured energy spectra, the Compton effect is seen by a broad continuum with an edge. The edge represents the energy deposition of a photon, which is scattered backwards so that the maximal energy is given to the electron (Compton-edge). The maximal energy transfer is given by:

$$E_{e,\mathrm{max}}' = \frac{E_\gamma}{1 + \frac{m_e c^2}{2E_\gamma}}. \tag{3.11}$$

The Compton effect is utilized for example in a Compton camera, which can be used to search for sources of γ-radiation.

Pair production

Photons carrying enough energy ($E_\gamma > 2m_e$) can be converted to an electron-positron pair in the Coulomb field of a nucleus or an electron [MG81]. The probability for pair production increases with Z^2 and - unlike the photoelectric and Compton effect - increases with increasing energy. Due to the small volume of the detectors used in this work, pair production can be neglected.

Examples of measured photon spectra

Fig. 3.8 shows the spectroscopic response of Timepix3 to the photon field of an ^{241}Am source. Three photopeaks can be found at 59.5 keV, 26 keV (γ-rays from the deexcitation of the excited daughter nucleus ^{237}Np*) and at 18 keV (superposition of Np L_β-lines).

The Compton effect can be seen by the energy depositions of the Compton electrons with the Compton edge at 11 keV and the tail of the 59.6 keV peak towards lower energies, which is partly due to Compton scattered photons absorbed in the sensor medium, and partly due to charge sharing losses to neighboring pixels, which are below the threshold.

18
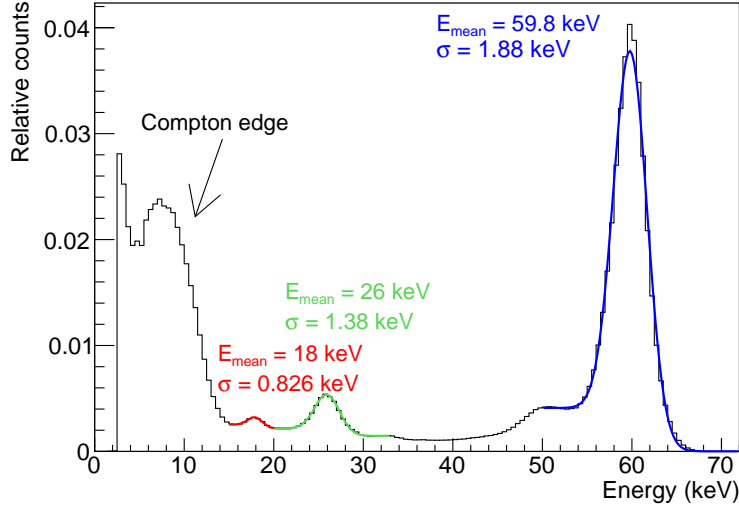
Figure 3.8: Photonic spectrum of an ^{241}Am source as recorded by a Timepix3 with 500 μm thick silicon sensor. The measured spectrum comprises of photopeaks due to γ-rays from the deexcitation of the ^{237}Np* at 59.5 keV and 26 keV and due to Np L_β photons. The 59.5 keV peak is accompanied by a tail towards lower energies caused by Compton scattered γ-rays and losses due to charge sharing. The Compton edge from the 59.5 keV γ-rays can be found at ≈ 11 keV.

As a further example, the measured energy spectrum of a ^{54}Mn source is presented in Fig. 3.9. ^{54}Mn decays to the excited state of ^{54}Cr*, which decays through the emission of an 835 keV γ-ray. Thus, according to eq. (3.11) the Compton edge should be seen at 638 keV, which is in close agreement with the experimentally determined value $E'_{e,\max} = (635 \pm 1)$ keV, when considering the energy resolution of 26 keV. The peak (at ≈ 780 keV), which looks like a photo-peak, is mainly due to electrons from internal conversion (the emitted γ-ray transfers its full energy to an electron of the atomic shell). However, even if the photoelectric effect is highly suppressed at the given energy, it could also include some photoelectrons produced in the silicon by the 835 keV γ-rays.

3.4 Neutrons

Since neutrons do not carry charge, they do not produce free charge carriers directly in the detection medium. Similar to photons, they have to be detected through ionization of secondary charged particles. However, whereas photons create a measurable signal through interactions with electrons in matter, neutrons mainly produce detectable secondary charged particles through interaction with the nuclei in the medium. Depending on neutron energy, different interactions are utilized for neutron detection.

Fast neutrons

In fast neutron fields ($T_n > 1$ MeV), elastic scattering off nuclei in the sensor material plays the major role. In neutron scattering, the energy transfer to a recoil nucleus T'_A in the medium is given by classic scattering theory:

$$T'_A = \frac{2A(1 - \cos(\theta_n))}{(A+1)^2} T_n. \tag{3.12}$$

19
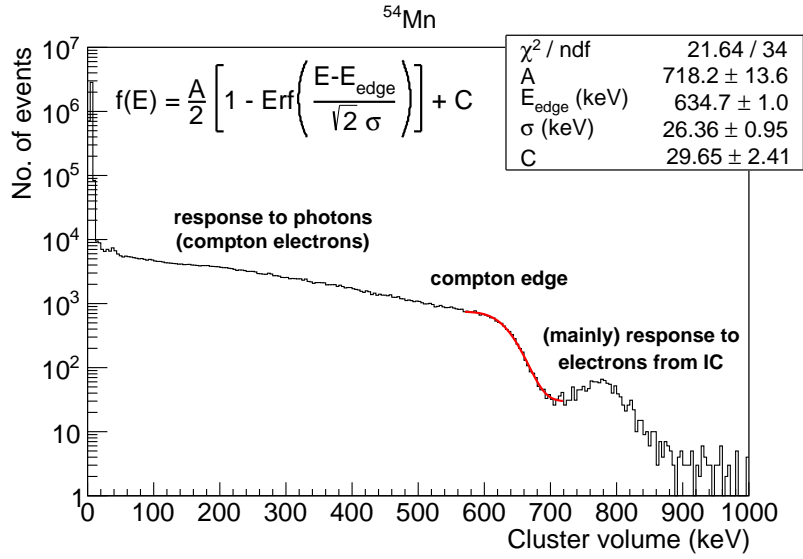
Figure 3.9: Spectrum of ^{54}Mn source as recorded with a Timepix3 with a 500 μm thick silicon sensor. The edge was found to be at (635 ± 1) keV by an S-curve fit. The energy resolution at this energy was found to be $\sigma_\text{E}(634\,\text{keV}) = 26.4\,\text{keV}$.

The maximal energy transfer to the medium is given by:

$$T'_{\text{A,max}} = \frac{4 T_\text{n} A}{A + 1},$$
(3.13)

where A is the atomic mass of the medium, T_n is the kinetic energy of the incident neutron and θ_n is the angle between the neutrons incident and scattered directions. In Eq. 3.13, it can be seen that energy absorption in the medium is most efficient for an absorber of low atomic mass. Thus, hydrogen rich materials (such as water, CH_2, Be, or graphite) are preferred for neutron conversion to charged particles and for moderation.

In Chapter 6, fast neutron scattering off silicon nuclei was further investigated and the ionizing energy losses of a recoil silicon ion on its path through the silicon lattice were determined by spectrum interpretation. Besides elastic scattering, fast neutrons also interact by inelastic scattering, where the nucleus of the medium is excited to a higher energy level, or by fragmentation, when a neutron induces a break-up of a nucleus in the absorber medium.

Cold, thermal and epithermal neutrons

For cold, thermal and epithermal neutrons, the main process for detection is neutron capture. Strongly absorbing materials are ^{3}He, ^{6}Li, ^{10}B, or ^{157}Gd[4]. Since the Q-values of the reactions are significantly higher than the neutron energies, with the energy resolution of typical detectors (Timepix in particular), the information about initial neutron energy gets lost in this process. Table 3.1 lists typical converter materials and reactions exploited for neutron detection.

3.5 Particle identification by basic pattern recognition

Depending on particle type and energy deposition, different characteristic cluster shapes can be observed. A categorization of such shapes was started in [HHJ$^+$08] considering data taken by a

---

[4] ^{3}He and ^{6}Li are the only nuclei, which absorb neutrons without γ-ray emission.

Reaction (energies in MeV)	Q-value [MeV]	Cross-section [b]
$^3\text{He} + {}^1\text{n} \rightarrow {}^3\text{H}\,(0.191) + {}^1\text{p}\,(0.573)$	0.764	5,333
$^6\text{Li} + {}^1\text{n} \rightarrow {}^3\text{H}\,(2.73) + {}^4\alpha\,(2.05)$	4.780	920
$^{10}\text{B} + {}^1\text{n} \rightarrow {}^7\text{Li}\,(1.015) + {}^4\alpha\,(1.777)$	2.792 (g.s., 6%)	3,837
$^{10}\text{B} + {}^1\text{n} \rightarrow {}^7\text{Li}^*\,(0.840) + {}^4\alpha(1.470)$	2.310 (1st exc. s., 94%)	3,837
$^{113}\text{Cd} + {}^1\text{n} \rightarrow {}^{114}\text{Cd} + \gamma\,(0.56) + \text{e}^-_{\text{conv.}}$	9.043 [RJKcv$^+$13]	20,600
$^{155}\text{Gd} + {}^1\text{n} \rightarrow {}^{156}\text{Gd} + \gamma\,(0.09, 0.20, 0.30) + \text{e}^-_{\text{conv.}}$	8.5 [KCM13]	60,600 [KCM13]
$^{157}\text{Gd} + {}^1\text{n} \rightarrow {}^{158}\text{Gd} + \gamma\,(0.08, 0.18, 0.28) + \text{e}^-_{\text{conv.}}$	7.9 [KCM13]	253,929 [KCM13]
$^{235}\text{U} + {}^1\text{n} \rightarrow$ fission fragments	210	583
$^{238}\text{Pu} + {}^1\text{n} \rightarrow$ fission fragments	160	748

Table 3.1: Overview of reactions and reaction products exploited for neutron detection. After [Owe12].
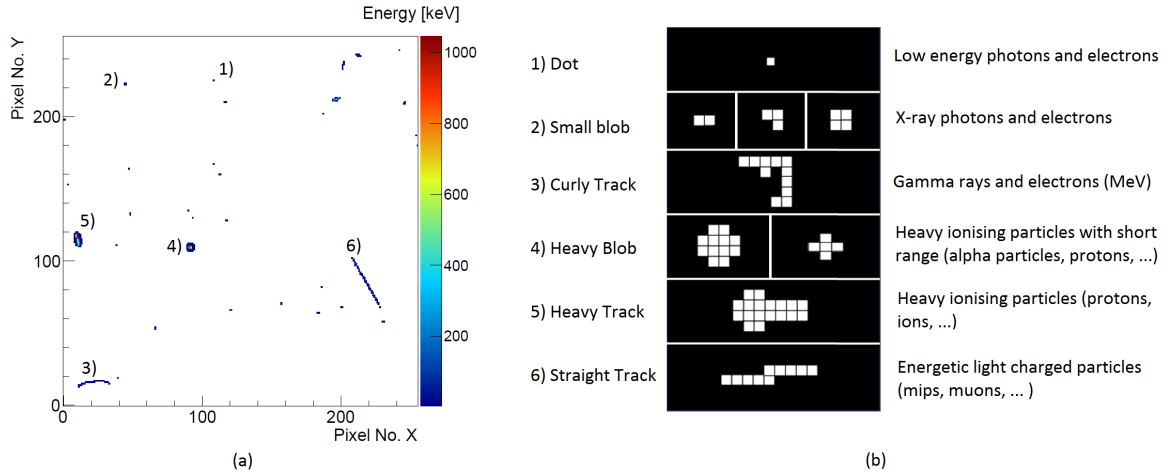
Figure 3.10: a) Frame of 10 s acquisition time in the natural background radiation at altitude 2,700 m. b) Classification scheme established by Holy [HHJ$^+$08].

Medipix2. It is based on morphologic cluster attributes, such as the relative number of pixels in a straight line, the deviation of the cluster from a circle, the number of inner pixels, and others. The defined categories with their possible origins are shown in Fig. 3.10.

Low energy electrons and secondary electrons from x-ray interactions deposit their energy in a small volume so that they are seen in few neighboring pixels. Thus, they are put to the categories "dot" and "small blob". Electrons and secondary electrons from the γ-ray interactions with higher ranges are characterized by tracks with random changes of direction (curly tracks). Particles passing through the sensor without deflection such as minimum ionizing particles (mips) create straight tracks.

Particles or interactions characterized by high charge creation in a small volume (α-particles, low energy protons, heavy ions) fall into the categories "heavy tracks" and "heavy blobs". They are also referred to as high energy transfer events.

For the neutron detection setup described in Chapter 5, this classification has proven valuable for separating interactions of highly ionizing charged particles (α-particles and tritons) from electron and γ-ray interactions.

However, since ionizing radiation covers a broad range of energies and particle species some ambiguities remain. For example a particle could be classified wrongly depending on the angle of

incidence: A mip impinging perpendicularly would be seen as a dot or as a small blob and thus be assigned to an x-ray interaction. Moreover, the categories of heavy tracks and heavy blobs include several particle species and energies (low energy α-particles up to relativistic ions). Therefore, for more accurate particle identification, other parameters available from the track should be considered, for example stopping power or distribution and initial direction of δ-rays. Improvements of the categorization scheme should be possible considering ongoing progress made in computer vision and artificial intelligence.

One particular limitation of Timepix technology is the inability to separate electrons and photons, since their 2D projections look identical. The development of Timepix3 however addresses this with the possibility to create voxelized 3D volumes (see Chapter 7), so that electrons would be seen as tracks starting from the edges, whereas γ-rays would create tracks starting at a random positions within the sensitive volume.

4 | Precision measurements of double K-shell vacancy creation during electron capture decays

The first application covered by the presented work is the detection of a rare coincident x-ray signal from double K-shell vacancy filling after the electron capture decay of an ^{55}Fe-source. These investigations led to a never-before achieved precision of the determination of the double K-vacancy production probability P_{KK} (Secs. 4.2 and 4.3) and the measurement of the angular distribution between the hypersatellite and the satellite photon (Sec. 4.3) for the first time ever.

4.1 Background

4.1.1 Double vacancy production probability

Electron capture is a well-known process. An electron from the atomic shell interacts with a proton in the nucleus, which is transformed to a neutron, while the Q-value of the decay is carried away by an electron neutrino. In the final state of the decay, the atom is thus left with a single vacancy in an atomic shell, which is filled by an electron from a higher shell along with the emission of an x-ray photon with an energy characteristic for the daughter nucleus and the involved shells. The probability of a K-shell capture is denoted P_{K} and was found to be $P_{\mathrm{K}} = 0.86$ for the investigated ^{55}Fe [BCD$^+$10].

Rarely, with probability P_{KK} in the order of $10^{-3} - 10^{-5}$, the second K-shell electron can be elevated to a bound state of higher energy (shake-up) or liberated to the continuum (shake-off). In the case of electron capture decays, the latter is the dominating process. Here, the shake-off electron can carry away energy up to approximately the Q-value of the decay [PC63]. A daughter atom with an empty K-shell (sometimes also referred to as a "hollow atom") is left behind. The process of a double K-shell vacancy creation is schematically shown in Figure 4.1.

The decay of such a double vacancy state $2s^{-2}$ proceeds either through the subsequent emission of 2 x-ray photons, the emission of 2 Auger electrons or the emission of one Auger electron and one x-ray photon. The photon emission probabilities are given by the flourescence yields ω_{K}. In the case of a double K-vacancy or a spectator vacancy in the L-shell, the fluorescence yield differs from that of a single vacancy [Che91, KBC02][1]. The photon emitted in the transition $1s^{-2} \to 1s^{-1}2p^{-1}$ is known as the "hypersatellite" photon, and the photon emitted in the transition $1s^{-1}2p^{-1} \to 2p^{-2}$ is the "satellite" photon. The energies of the emitted x-rays are shifted to higher energies compared to the K-line photons, due to the reduced screening of the Coulomb potential [BCTR71, BCJ$^+$74], either by a "spectator" vacancy in the K-shell (hypersatellite) or the L-shell (satellite). A 2-photon decay of an initial double (K-shell) vacancy state is illustratively shown in Fig. 4.2.

---

[1] In most publications on this topic, and also the work presented in Section 4.2, this has not been taken into account.
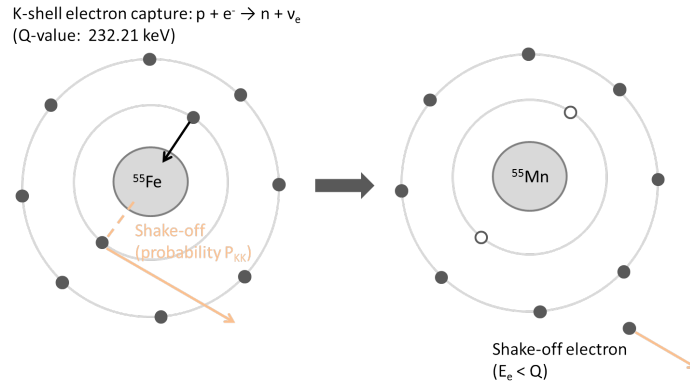
Figure 4.1: Schematic illustration of the creation of a double K-vacancy in the electron capture decay of ^{55}Fe.
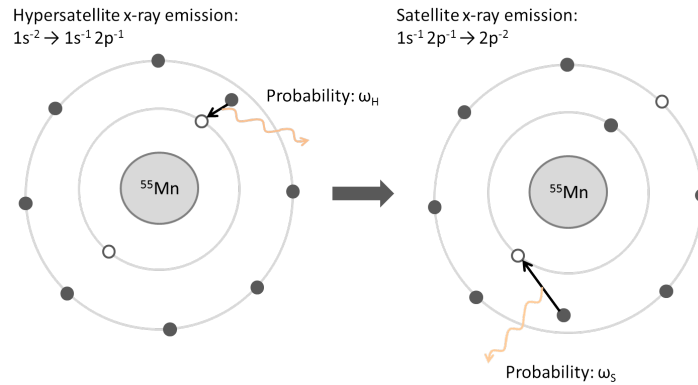
Figure 4.2: Schematic illustration of the decay of a double K-shell vacancy state.

The pioneering work of Charpak [Cha53], who determined P_{KK} for ^{55}Fe with two gaseous detectors, was followed by further investigation including other nuclei. Most commonly, energy-sensitive detectors (NaI or Ge) were employed in a coincidence setup. The data demonstrated the overall tendency of P_{KK} to decrease with Z^{-2}, as predicted by the Primakoff-Porter theory [PP53]. Hindi and Kozub [HK91] gave an overview of experimental results, but also claimed that theoretical data do not match the measured values well and that experimental data lacks the precision required to draw decisive conclusions on which models to prefer. This is especially true for the investigated ^{55}Fe, where P_{KK} was determined to be $(1.3 \pm 0.2) \times 10^{-4}$ by Campbell et al [CMT91]. When compared to the P_{KK} calculation approaches shown in Table 4.1, the value favors the Coulomb propagator method. Still, two other models lie within a 3σ confidence interval. Two of the models could be excluded, being further away than 5σ from the measured value. Additionally, compared with the P_{KK} results of the neighboring ^{54}Mn [HWK03] and ^{65}Zn [NS83], deviation from the predicted Z^{-2} behavior occurs. This deviation might be explained by the fact that ^{55}Fe almost exclusively decays to the ground state, whereas the other two isotopes decay to excited states of the daughter nuclei. Here, internal conversion in the K-shell, inherently producing a double K-shell vacancy, could be confused with double vacancy creation by electron capture.

Section 4.3 discusses its effect and corrects the results of previous works.

$P_{\mathrm{KK}}[\times 10^4]$	Method
4.8	Correlation effects neglected
0.881	Initial state correlation effects corrected
1.13	Coulomb propagator method
2.4	SCF potential plus final state correlation
0.904	Correlation-split wave function

Table 4.1: Overview of P_{KK} values calculated by different theoretical approaches for ^{55}Fe. After [CMT91].

4.1.2 Angular correlation measurement

Up to now, the angular correlation between the emitted satellite and hypersatellite photons has not been studied. The angular correlation could be a significant source of uncertainty for the interpretation of the results for the double vacancy production probability especially in coincidence experiments, where the solid angle is not fully covered.

Additionally, in angular correlation measurements, information can be gained about the shell structure and transition probabilities in many-electron atoms and ions. They are also a tool to investigate admixtures of higher electric or magnetic moments of the radiation emitted in the decay of a given shell configuration. In addition, angular correlation measurements can provide information about relativistic effects.

The decay of the double vacancy state to the ground state of the atom can be regarded as the two-step process

$$
\begin{aligned}
\left|1s^{-2}:J_a\right\rangle &\rightarrow \left|1s^{-1}2p^{-1}:J_b\right\rangle + \gamma_{\mathrm{HS}} \\
&\rightarrow \left|2p^{-2}:J_c\right\rangle + \gamma_{\mathrm{HS}} + \gamma_{\mathrm{S}},
\end{aligned}
\tag{4.1}
$$

where J_a, J_b, and J_c denote the total angular momenta of the initial state, the intermediate state and the final state, respectively. The angular distribution of the radiative decay emitting the satellite photon can then be described by

$$
W(\theta) = \frac{\sigma_0^{\mathrm{dec}}}{4\pi}\left(1 - \sum_{k=2,4,\ldots} f_k^{\mathrm{dec}}(J_b,J_c) \times \mathscr{A}_{k0}(J_b)P_k(cos\theta)\right),
\tag{4.2}
$$

where σ_0^{dec} is the total decay rate, θ is the angle of the satellite with respect to the hypersatellite photon, $\mathscr{A}_{k0}$ is the statistical tensor, which is sensitive to the sublevel occupation of the excited states and, $f_k^{\mathrm{dec}}(J_b,J_c)$ is the so-called anisotropy parameter, which purely reflects the electronic structure of the ion [SJSF06]. For the low- and medium-Z elements, a mixing of multipole transitions was reported to be negligible, so that electric-dipole behavior is commonly assumed. The angular correlation function in electric dipole approximation is simplified to:

$$
W(\theta) = \frac{\sigma_0^{\mathrm{dec}}}{4\pi}\left(1 - f_2^{\mathrm{dec}}(J_b,J_c;E1) \times \mathscr{A}_{20}(J_b)P_2(cos\theta)\right)
\tag{4.3}
$$

where the anisotropy parameter is given by:

$$
f_2^{\mathrm{dec}}(J_b,J_c;E1) = (-1)^{1+J_b+J_c}\sqrt{\frac{3\,(2\,J_b+1)}{2}}\left\{\begin{array}{ccc} 1 & 1 & 2 \\ J_b & J_b & J_c \end{array}\right\}.
\tag{4.4}
$$

Further discussion and the application of the formulae to the hypersatellite-satellite cascade for the investigated isotope ^{55}Fe is given in Sec. 4.3.
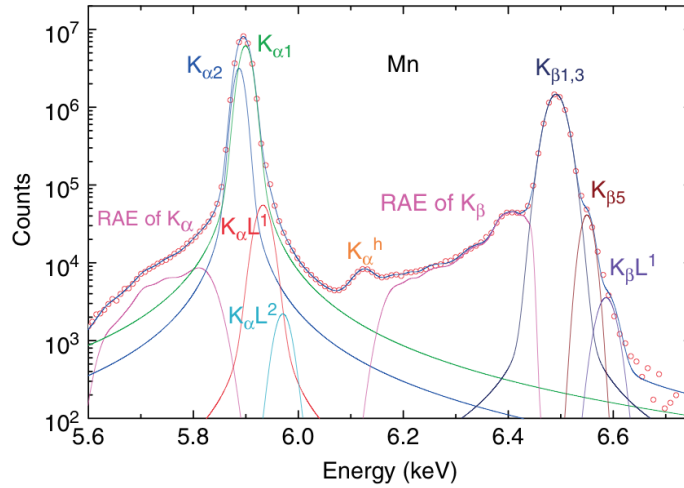
Figure 4.3: Spectrum of x-ray emissions of Mn. From [MSBN08]

4.1.3 Measurement concept with the Timepix

In the presented work, a stack consisting of two Timepix detectors was utilized to measure P_{KK}. However, the Timepix lacks the energy resolution to separate the hypersatellite from the flourescence line photons. The ^{55}Mn spectrum shown in Fig. 4.3 shows that the energy resolution has to be significantly below 0.5 keV to be able to separate the hypersatellite line from the K-line photons. The resolution of the Timepix at 6 keV (in the ToT mode) is $> \approx 3$ keV (FWHM). Thus, an experimental attempt was made to determine P_{KK} relying solely on coincidence information. Although the experiment was first designed as a proof-of-principle, it soon became clear that the Timepix stack was a suitable candidate to increase the precision of P_{KK}, and, thanks to its segmentation, to determine the angular correlation function between the hypersatellite and satellite photon.

A major disadvantage of the measurement was the high relative amount of dead time resulting in long measurement times (approximately 2 years). Special care has to be taken to ensure stable conditions for long measurement times. This is especially pertinent considering potential damage in permanently irradiated radiation detectors, which alters their properties leading to increased noise or a lower charge collection efficiency (thus resulting in smaller x-ray detection efficiencies). Short measurement times can be achieved with the data-driven readout scheme implemented in the Timepix3 detectors. Moreover, since Timepix3 offers the simultaneous measurement of time and energy, unwanted coincident background events, which must be subtracted (relying on literature constants and energy spectra presented elsewhere as simulation inpu), could (at least partly) be identified and eliminated, thus significantly reducing the systematic error. With the energy information available, measurements with electron capture isotopes decaying to the excited state of the daughter nucleus would become feasible. Here, double K-shell vacancy states are not only produced in shake processes, but also through internal conversion of the γ-ray from the deexcitation of the nucleus on the remaining K-shell electron.

4.2 Publication: Measurement of the double K-shell vacancy creation probability in the electron-capture decay of ^{55}Fe with active-pixel detectors

The following work was published as "Measurement of the double K-shell vacancy creation probability in the electron-capture decay of ^{55}Fe with active-pixel detectors" by T. Michel, B. Bergmann, J. Durst, M. Filipenko, T. Gleixner, and K. Zuber in Physical Review C89 (2014) no.1, 014609. Doi: 10.1103/PhysRevC.89.014609

A stack consisting of two Timepix hybrid pixel detectors facing each other with the radioactive source in between was used for high precision measurement of the double K-shell vacancy production probability P_{KK} in the electron capture decay of ^{55}Fe. P_{KK} was determined for the first time in a pure coincident event counting experiment without energy information. The main achievements were the following:

- The methodology for the P_{KK} determination with Timepix pixel detectors was developed and described. Coincident background processes which cannot be discriminated against (without energy information) were identified and their impact on the measurement results was estimated in simulations using probabilities and energy spectra (where available) found in literature as input parameters;

- $P_{KK} = (1.531 \pm 0.079)^{-4}$ was measured, with a systematic uncertainty of $(\Delta P_{KK})_{\text{syst.}} = 0.023 \times 10^{-4}$. This result was the highest accuracy ever achieved, at the time of publication. To date, a higher precision has only been achieved with the publication presented in Sec. 4.3, where the same evaluation technique was used;

- The P_{KK} result was discussed with respect to other measurements on ^{55}Fe and, using the Primakoff-Porter scaling law, with the neighboring electron capture isotopes ^{54}Mn and ^{65}Zn. Agreement to previous measurements on ^{55}Fe was found. The ratio of P_{KK} for ^{54}Mn and ^{55}Fe was consistent with 1 on a 1σ level. Still, the value for ^{64}Zn deviates from the Z^{-2} trend. In Sec. 4.3, the trend was confirmed with higher precision data, additionally taking into account the differing flourescence yields of the single and double vacancy states.

My own contribution to the publication:

- Data analysis;

- Interpretation of the physical results together with T. Michel;

- Design of the measurement setup;

- Detector preparation;

- Data acquisition;

- Development of the methodology for data evaluation (together with T. Michel);

- Simulation of the detector responses and detection yields;

- Contribution to the writing of the publication.

Other author's contribution to the publication:

- Writing of the publication (T. Michel);

- Help with the detector preparation;

- Development and support on the simulation-framework;

- Development of the methodology for the data evaluation (T. Michel and B. Bergmann);

- General discussions.

4.3 Publication: Angular correlation function of the hypersatellite-satellite x-ray cascade following the electron capture decay of ^{55}Fe

The following work was published as "Angular correlation function of the hypersatellite-satellite x-ray cascade following the electron capture decay of ^{55}Fe" by B. Bergmann, T. Michel, A. Surzhykov, and S. Fritzsche in Physical Review C94, 014611 (2016). Doi: 10.1103/PhysRevC.94.014611

It is the continuation of the work started in Sec. 4.2. With the higher amount of data measured, P_{KK} in the electron capture decay of ^{55}Fe was determined with an up to now unprecedented accuracy. Additionally, the angular correlation function of the hypersatellite and satellite emissions was measured for the first time. The work covers the following improvements:

- The double vacancy production probability ^{55}Fe was determined to be $P_{\mathrm{KK}} = (1.388 \pm 0.037) \times 10^{-4}$, with systematic uncertainty $(\Delta P_{\mathrm{KK}})_{\mathrm{syst.}} = 0.042 \times 10^{-4}$. The different flourescence yields of the double and single vacancy state were taken into account for the first time in such an evaluation. Compared to the publication presented in Sec. 4.2, also the angular correlation between the hypersatellite and the satellite photon were considered for simulation of detection yields;

- The ^{55}Fe result obtained was compared with previous measurements on ^{55}Fe and the neighboring electron capture isotopes ^{54}Mn and ^{65}Zn. Hereby, the assumption of equal flourescence yields in the single and double vacancy state made by all other works was corrected for. Agreement was found with previous results of ^{55}Fe and on an almost 1σ level with the value measured on ^{54}Mn. For ^{65}Zn the discrepancy remained;

- A measurement of angular correlation function of the hypersatellite satellite cascade was presented for the first time. The anisotropy parameter $\beta_2^{\mathrm{eff}}(\mathrm{exp.}) = 0.097 \pm 0.053$ was determined, which can be compared with the value calculated in electric dipole approximation $\beta_2^{\mathrm{eff}}(\mathrm{theor.}) = 0.09735$.

My own contribution to the work:

- Data analysis;

- Interpretation of the data in order to obtain the physics results (together with T. Michel);

- Design of the measurement setup;

- Detector preparation;

- Development of a methodology for data evaluation (together with T. Michel);

- Simulation of the detector response and detection yields;

- Writing of the publication.

Co-authors' contributions:

- Theoretical calculation of the anisotropy parameter (A. Surzhykov and S. Fritzsche);

- Development of the methodology for the data evaluation (T. Michel and B. Bergmann);

- Contribution to the writing;

- General discussions.

5 | Neutron detection with Timepix

5.1 Background

5.1.1 Conventional neutron detectors

Neutron detection occurs through the detection of secondary particles following neutron capture (mainly thermal) or recoils from neutron scattering (fast neutrons).

The gold standard for thermal neutrons is a ^{3}He tube, which is essentially a proportional counter filled with pressurized ^{3}He gas [KEE$^+$10]. Ionization is produced by the proton and the ^{3}H from the ^{3}He(n,p)^{3}H reaction. The same detection principle is used in the BF$_3$ tube, fission chamber, and the GEM detector [PMC$^+$13]. In order to increase the sensitivity to neutrons of higher energies, gas proportional counters are surrounded by a hydrogen-rich material, which moderates the incident neutrons to thermal energies (where the capture cross section is the highest). Depending on the moderator thickness the detectors have differing energy responses. In a system combining such moderation detectors (for example the Bonner Sphere Spectrometer [bss, BEB60]), a deconvolution method can be used to determine the incident neutron energy spectrum. Alternative ways of recording neutron spectra utilize the time-of-flight information or (for fast neutrons) the recoil proton technique [DBB$^+$10].

Other commonly used neutron detectors are activation foils, nuclear track detectors, plastic scintillators and bubble detectors [Peu00]. Their working principles are briefly outlined in the following:

- **Activation foils** are activated during neutron impact. A determination of the γ or β-emission rates in the decay of created radioactive isotopes is a measure of the neutron fluxes. A proper foil material has to be chosen in order to be sensitive to the given neutron spectrum (see [act]). Silver, indium, and gold are used in thermal neutron fields, whereas iron, magnesium, or aluminum can be used for fast neutron detection.

- **Plastic scintillators:** In scintillation detectors secondary particles after neutron interactions (typically recoil protons after fast neutron impact) create visible light, which is then detected in photomultiplier tubes (PMTs). To enhance their sensitivity to thermal neutrons they can be loaded with ^{3}He or ^{10}B. However, large footprints are required for reasonable detection efficiencies [HOvdB14].

- **Nuclear track detectors (NTD):** Charged particles passing through dielectric material create submicrometer-sized defects along their trajectory [ntd]. These defects can be made visible for analysis using chemical etching techniques. A proper characterization of shape and orientation can give the LET of the incident particle. When exploited for neutron detection, they typically record the tracks of recoil proton, recoil carbon or recoil oxygen after fast neutron impact. To enhance detection efficiencies, they are sometimes equipped with a radiator. The energy deposition of electrons is rather low so that no significant damage is created. Thus,

the electron and γ-ray background is inherently suppressed. Even though they are a cost-efficient approach for neutron detection, they come with the drawback of being passive and prone to overexposure (defect density is too high to identify individual tracks). Besides neutron detection, these foils have found an application in the MoEDAL experiment, searching for the Dirac monopole at the LHCb at CERN [Pin17].

- **Bubble detectors** contain a suspension full of microscopic liquid droplets. By pressurizing (depressurizing) the suspension, the detector is activated (deactivated) [bub]. When neutrons hit the droplets, visible bubbles of trapped gas form immediately, which can be counted by eye or in a reader. Multiplying the number of bubbles with a calibration coefficient indicates the dose level of the surrounding neutron field. Similarly to NTDs, γ-rays or electrons cannot produce a signal. Using different liquids, sensitivity to different neutron energy ranges can be achieved. Bubble detectors are found in radiation protection, where they are used as a quasi-active neutron dosimeter. Besides neutron detection, thanks to their good background suppression, they were found to be valuable in experiments searching for dark matter [HLR$^+$97].

5.1.2 What's the use of a new detector?

The main drawbacks of the described systems are that they are either passive, unhandy, or a primary knowledge of the neutron field is required. Consider the situation of monitoring the neutron fluxes in a control room. The neutron spectrum would strongly depend on the number of "moderating objects" (in this case humans) in the room.

The aim of this work was to develop an active, compact neutron detection system able to discriminate neutrons against charged particles and γ-rays in a mixed radiation field, while also being sensitive to a wide range of neutron energies (thermal, fast). Additionally, crude spectroscopic information should be provided. The presented device was designed for one of the most challenging man-made mixed radiation fields, the ATLAS detector. However, the device's applications are not restricted to the ATLAS cavern. Neutron environments (and mixed radiation fields) can be found at nuclear power plants, around particle accelerators, or in medical facilities. Recently, particle therapy has become popular for the treatment of cancer, due to the advantage of delivering high radiation doses to carcinogenic tissue while keeping the damage to the surrounding tissue low. During treatment, secondary neutrons are created, which can increase the doses of ionizing radiation to the patient and have to be considered for beam line optimization (shielding, neutron activation, etc.). Depending on the primary beam and its energy, the produced neutron spectra can be rather hard. Additionally, these neutrons have to be discriminated against charged fragments [PANJ09, JGH$^+$11, MJG$^+$11].

The first iteration of the neutron detector consisted of a single layer Timepix with a set of neutron converters attached to it (Sec. 5.2). Using a basic pattern recognition approach, this design allows a proper separation of neutron interactions from γ-rays and electrons. Section 5.3 then describes a two-layer approach to improve the separation of neutron events from charged particle events by utilizing coincidence (or anticoincidence) behavior and assessing the directionality of the fast neutron component. In Sec. 5.4, the first results of the measurement of the thermal neutron component at various places in the ATLAS detector are shown. Further research should focus on a reduction of weight and power consumption to create a neutron detector, which would be highly valuable for neutron dosimetry or for space missions, where it can be used for example for water searches by means of moderated neutron detection or to monitor and study solar flares of γ-ray bursts [HOvdB14].

5.2 Publication: Time-of-flight measurement of fast neutrons with Timepix detectors

The following article was published as "Time-of-flight measurement of fast neutrons with Timepix detectors" by B. Bergmann, R.O. Nelson, J.M. O'Donnell, S. Pospisil, J. Solc, H. Takai, and Z. Vykydal as an IWORID conference proceeding in the Journal of Instrumentation 9, C05048, 2014. Doi: 10.1088/1748-0221/9/05/C05048

This was the starting point of the research focused towards the development of an active neutron detection system covering a broad energy range from thermal to fast neutrons. The detection system should be lightweight and easy to handle (in contrast to the widely used Bonner spheres) and give the results in real-time (in contrast to the nuclear track detectors and activation foils). Therefore, the capabilities of a Timepix hybrid pixel detector for fast neutron detection were investigated in a time-of-flight experiment at a spallation neutron source in the Los Alamos Neutron Science Center. In order to detect neutrons, ^{6}Li (89 % enrichment) and polyethylene (approximately 1.2 mm thick) were used as converter materials. The following list summarizes the main outcomes:

- The publication covers the selection of appropriate converter foils/materials for fast neutron detection and spectral fast neutron field characterization. In particular, it presents the detector responses and efficiencies to neutron impact (energy range 1 MeV-600 MeV) for different converter materials;

- In order to assign the detector responses to (quasi-)monochromatic neutrons, the time-of-flight methodology was adapted for the use with the ToA mode of the Timepix detectors. The developed algorithm was the foundation of the publications presented in Sec. 5.3 and Sec. 6.2 of this work and referred to by George [Geo15].

- The work illustrates how highly ionizing particles (protons, α-particles, etc.) produced in the converter material or the silicon itself can be separated from γ-ray interaction by a pattern recognition algorithm. By examining track characteristics, it was found that the ratio of tracks with elliptical shape to tracks with round shape decreases with increasing neutron energy (above 30 MeV). It was suggested to make use of this ratio to assess the neutron energy in the range where the converters are not sensitive anymore;

- The obtained response functions allowed a validation of the MCNPX simulation, presented in [CHL$^+$13], which was a crucial input for the study of the radiation fields' composition in the ATLAS experiment and benchmarking of ATLAS simulations.

My own contribution to the work:

- Detector preparation;

- Responsibility for the measurement;

- Development of the methodology for the data evaluation;

- Interpretation of the physical results;

- Data analysis;

- Writing of the publication.

Co-authors' contributions:

- MCNPX simulation of the detector response to neutrons (J. Solc);

- Preparation of the beam time proposal;

- Beam line support;

- Design and assembly of the measurement setup;

- Participation at the measurement;

- General discussions.

5.3 Publication: ATLAS-TPX: a two-layer pixel detector setup for neutron detection and radiation field characterization

The following article was published as "ATLAS-TPX: a two-layer pixel detector setup for neutron detection and radiation field characterization" by B. Bergmann, I. Caicedo, C. Leroy, S. Pospisil, and Z. Vykydal in the Journal of Instrumentation 11, P10002, 2016. Doi: 10.1088/1748-0221/11/10/P10002

Based on the experience gained in Sec 5.2 and the results from the ATLAS-MPX network [CHL⁺13], the neutron detection system was modified in order to improve the capability of particle species separation and to determine a prevailing direction of the fast neutron component by simultaneously increasing the solid angle acceptance. For this purpose, a stack consisting of two Timepix detectors with a set of neutron converters in between was used.

Thermal neutrons were registered below a $1.6\,\mathrm{mg/cm^2}$ thick ^{6}Li (89 % enrichment) layer while fast neutrons were detected through recoil protons from a polyethylene layer. In order to gather spectral information of the fast neutron field, a thin aluminum foil was inserted below one half of the polyethylene, stopping recoil protons of too low energy. The applicability of the (anti-)coincidence technique of the device and the detector responses to charged particles were determined in proton and ion beams at the Heidelberg Ion Therapy Center. The neutron detection efficiencies and detector responses are presented for a thermal neutron field, standard radionuclei sources (Am-Be, ^{252}Cf) and neutron beams (Van-de-Graaff accelerator in Prague, a spallation source in the Los Alamos Neutron Science Center). The publication covers the following points:

- The (anti-)coincidence technique was introduced as a tool to separate charged particles (coincidences) from neutrons (anticoincidences) and studied. The probabilities of charged particles to be seen in coincidence was given as a function of the impact angle. For neutrons, the anticoincidence behavior was determined as a function of neutron energy. It was found that neutrons with energies above 20 MeV can also create coincidences due to the extended range of the products of spallation reactions;

- It was shown that the ratio of the signal below the polyethylene and the polyethylene region with additional aluminum foil can indicate the neutron energy in the range 1 MeV-20 MeV;

- The anisotropy of the (fast) neutron signal with respect to the layers was used to assess the directionality of the fast neutron component;

- Simulation data, obtained with a detailed Geant4 simulation, were validated against the experimentally determined responses;

- Data analyses in different typical use cases (mixed radiation fields) were presented. These included the reduction of the neutron flux by material in a neutron beam, the monitoring of the rates of charged particles and neutrons at a beam line and behind a phantom in particle therapy.

My own contribution to the work:

- Simulation of the detector response to neutrons;

- Preparation of beam time proposals;

- Development of the methodology for the data evaluation;

- Experimental testing;

- Data analysis;

- Interpretation of physical results;

- Writing of the publication.

Co-authors' contributions:

- Preparation of beam time proposals;

- Detector preparation;

- Experimental testing;

- Design and assembly of the measurement setup;

- General discussions.

5.4 Application: The ATLAS-TPX detector network

16 ATLAS-TPX devices were installed in the ATLAS experiment and the ATLAS control room, where they are used to provide real-time characterization of the radiation field and measurement of neutron fluences. Devices closer to the interaction points are in a rather harsh radiation environment. Therefore, radiation sensitive electronics had to be separated from the actual detector. This section describes how the devices were calibrated for their neutron efficiencies, how the data were acquired, and gives first results.

5.4.1 Calibration of the neutron detection efficiencies

Before installation, each device was calibrated in an isotropic thermal neutron field created by the moderation of fast neutrons from multiple Pu-Be sources in a large graphite pile at room temperature ($E_n \approx 25\,\text{meV}$) and in the neutron field of a ^{252}Cf-source ($\langle E_n \rangle = 2.2\,\text{MeV}$). The results of the thermal neutron efficiency calibrations are given in Fig. 5.1. The results of the fast neutron calibration in Fig. 5.2. A mean thermal neutron efficiency $\langle \epsilon_{\text{th}} \rangle = 0.56\,\%$ was found. Deviations from the mean value occur due to the different thicknesses and extensions of the ^{6}LiF-layer, which were sprayed manually onto aluminum foils. However, this demonstrates a reproducibility of this procedure within a relative $\sigma_{\text{rel.,thermal}}$ of $\approx 20\%$.

The fast neutron efficiencies are distributed around the mean $\langle \epsilon_f \rangle = 0.043\,\%$ with a standard deviation of $\sigma_{\epsilon_{\text{fast}}} = 0.0025\%$ ($\sigma_{\text{rel.,fast}} \approx 10\%$).

5.4.2 Device positions and operation in the ATLAS Cavern

The 16 calibrated devices were installed at different positions in the ATLAS cavern at the positions given in Fig. 5.3b and Table 5.1. Devices close to the interaction points (TPX01-TPX04 and TPX11-TPX14) were placed symmetrically on side A and side C of the ATLAS experiment. To protect the active electronics in the readout system from radiation damage, they are separated from the actual detector and situated in the rack room outside the ATLAS cavern (USA 15). The devices and the readout systems are connected to each other through three Ethernet cables (see Fig. 5.3a), with cable lengths of up to 90 m (TPX09). A fourth cable is used for providing the bias voltage to the two layers.
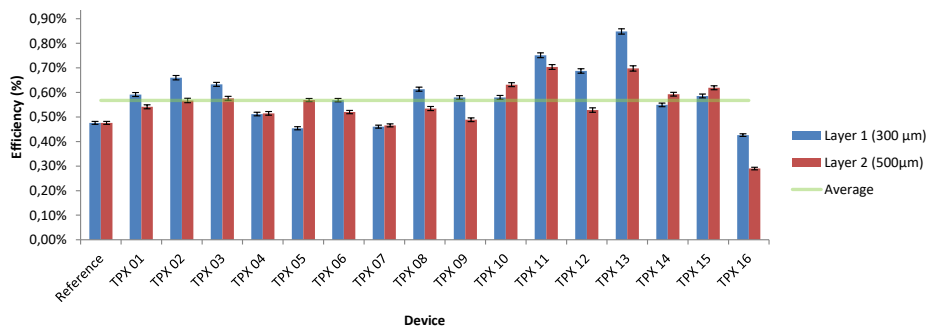
Figure 5.1: Results of thermal neutron ($\approx 25\,\text{meV}$) efficiency calibrations for 17 ATLAS-TPX devices (16 of which were installed in the ATLAS experiment and one is used as a reference device). Thermal neutrons are detected by α-particles and ^{3}H created in ^{6}LiF layers of thickness $(1.3 \pm 0.3)\,\text{mg/cm}^2$ (enrichment: 89 %). The blue bars and the red bars correspond to the values measured for the 300 μm and 500 μm thick sensor layers, respectively.

Table 5.1: Overview of the positions of the ATLAS-TPX devices in the ATLAS experiment with respect to the interaction point, cable lengths, and frame rates. After the assembly of the surrounding structures, no connection to the TPX10 could be established.

Device	X [mm]	Y [mm]	Z [mm]	Cable length [m]	Frame rate (s^{-1})
TPX01	670	880	3540	81	6.76
TPX02	-1100	180	3540	73	8.33
TPX03	150	-1130	3540	74	6.76
TPX04	-3580	970	2830	47	8.33
TPX05	1320	-494	7830	82	8.33
TPX06	2370	-1030	7830	81	8.33
TPX07	3300	-1590	7830	80	8.33
TPX08	-6140	0	7220	51	8.33
TPX09	0	1560	15390	90	2.7
TPX10	230	440	18859	-	-
TPX11	660	900	-3540	84	6.76
TPX12	-930	670	-3540	77	8.33
TPX13	90	-1100	-3540	76	8.33
TPX14	-3580	970	-2830	49	8.33
TPX15	-16690	50	5020	40	8.33
TPX16	-18900	50	5020	24	8.33

The readout consists of two main parts:

- An FPGA[1] for control of the device settings and operation, and;

- a Raspberry PI minicomputer for data conversion to a human readable format and communication to the control unit.

In principle, a readout speed of up to 30 frames per second (fps) could be achieved. However, to account for extended cable lengths, the devices are operated at lower rates. Table 5.1 summarizes the detector positions, the cable lengths, and the achieved frame rates. During the assembly of the ATLAS structures around TPX10, its cable connection was damaged, so that is was not possible to establish a connection to this device.
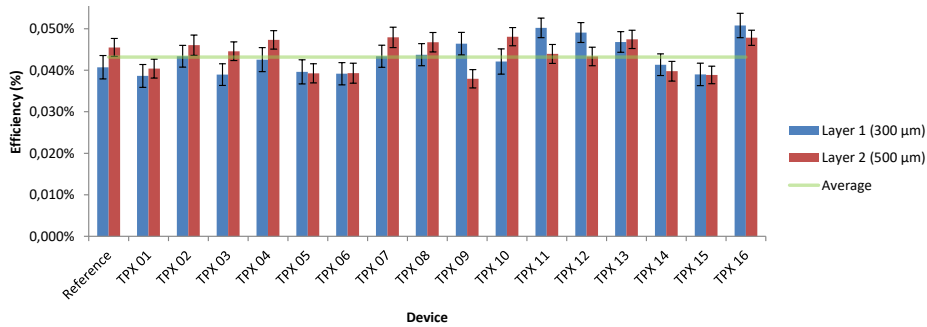
---

[1]Field Programmable Gate Array

Figure 5.2: Same as Fig. 5.1, but for the fast neutrons of a ^{252}Cf-source ($\langle E_n \rangle = 2.2$ MeV). The neutrons were seen below the PE converters.
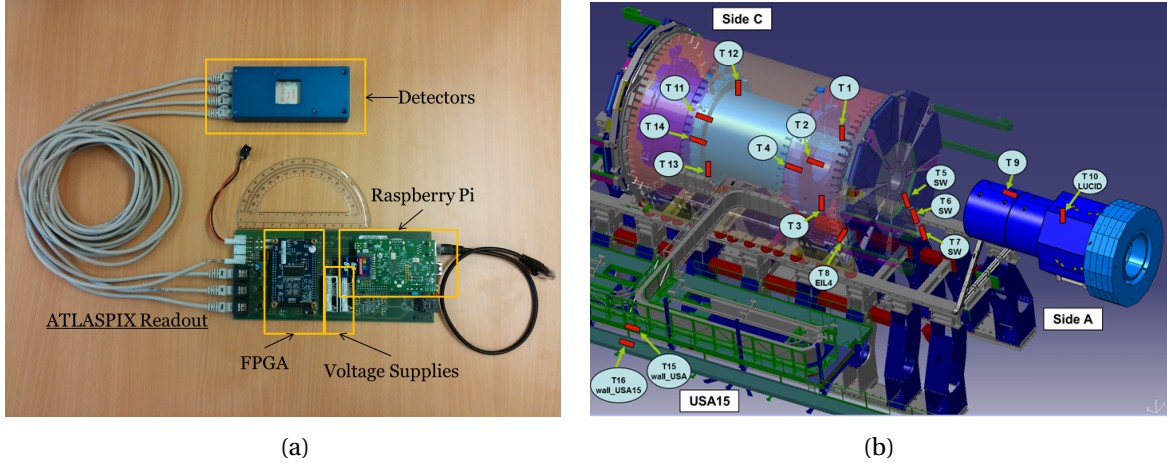
Figure 5.3: (a) ATLAS-TPX device, connected to its readout system through three Ethernet cables. The readout system consists of an FPGA, handling the device settings and operation, and a Raspberry Pi minicomputer for sending the data to the control PC in human readable format. Two voltage supplies are used for feeding the proper bias to each of the sensor layers; (b) Artistic view of the device positions of the ATLAS-TPX network in the ATLAS experiment.

5.4.3 Typical frames

Figures 5.4a-5.4d show frames from TPX01, TPX03, TPX07, and TPX09, respectively. They illustrate the detector responses to the radiation fields seen by these devices. For the determination of the field composition, individual tracks must be identified. Therefore, short frame exposure times were used in the detectors close to the interaction point (TPX01, TPX03, TPX11, and TPX13). In this setting, the ratio of the frame acquisition time to readout (dead) time is $\frac{t_{\text{life}}}{t_{\text{dead}}} \approx 0.2\,\%$.

The dominating interactions in all devices are characterized by a low energy transfer to the detectors, which is typical for γ-rays, electrons or minimum ionizing particles. The rate of highly ionizing particles is significantly lower. In the detector response of TPX09 (Fig. 5.4d), aligned tracks (mainly parallel to the y-axis) can be seen. Due to a horizontal alignment of the TPX09 with respect to the beam, muon tracks from the interaction point hit the sensors at relatively high angles with respect to the sensor normal, thus producing long traces.

5.4.4 Measurement of the thermal neutron fluxes

The data evaluation of the thermal neutron fluxes, as measured during LHC Fill 4965 on May 31, 2016 (Run 300,571, peak luminosity $6.8 \times 10^{33}\,\text{cm}^{-2}\text{s}^{-1}$) is addressed in the following as a typical example. Integral frames of HETE are shown in Fig. 5.5 for different detectors. The thermal neutron region was found to show an excess in count rates.

The thermal neutron flux determination is discussed in the following. The energy deposition spectra of HETEs below the ^{6}LiF and the uncovered region are compared to illustrate the effect of the ^{6}LiF converter and to document that the measured signal is due to the conversion of thermal neutrons. This is depicted for two different devices: for TPX01 in Fig. 5.6a and for TPX07 in Fig. 5.6b. The spectra show the integrated signal for the whole day May 31, 2016. This corresponds to a total measurement live time of 164 s for TPX01, and 9.5 hours for TPX14, respectively. After subtraction of the spectra in the uncovered regions, the peaks of α-particles (at energy $E_{\text{dep.}} \approx 1\,\text{MeV}$) and ^{3}H (at energy $E_{\text{dep.}} \approx 2.5\,\text{MeV}$) remain. These can be directly compared to the spectra shown in Section 5.3. In particular the ^{3}H-peak can also be valuable for a long-term (period of device operation) systematic study of the radiation damage of the silicon sensor, for example when evaluating the

39
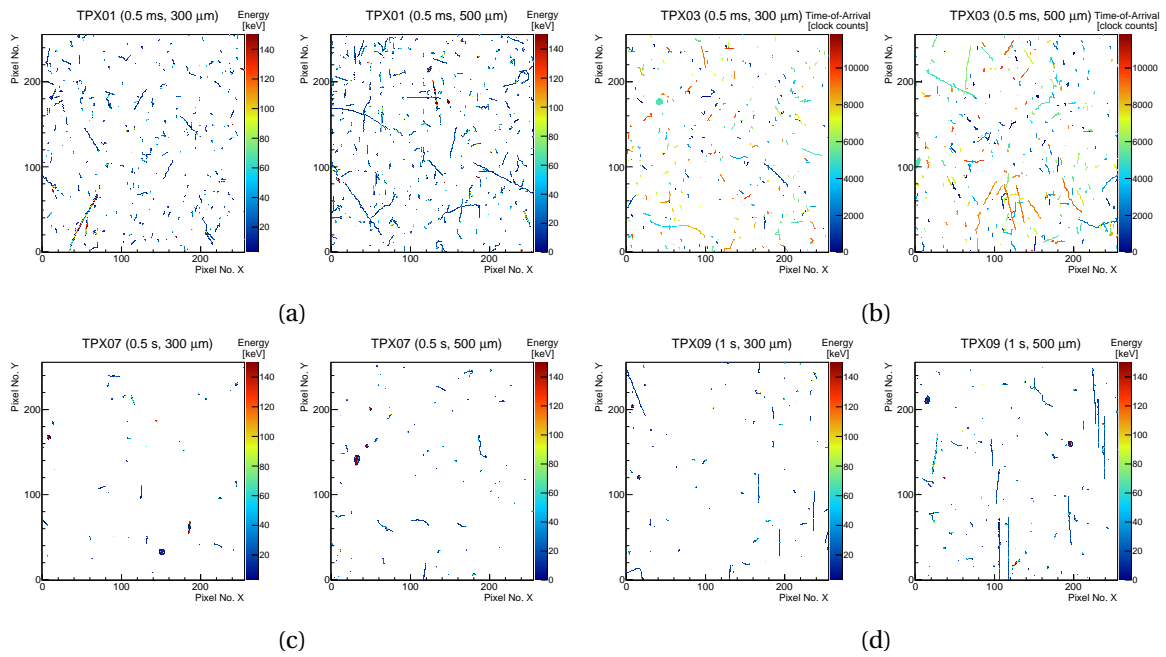
Figure 5.4: Characteristic frames measured during Run300541 on May 31. (a) Frame of 0.5 ms frame exposure time recorded by the detector TPX01. The detector was used in ToT mode. The color in each pixel represents the energy deposited during the exposure time; (b) Frame of 0.5 ms frame exposure time recorded by the detector TPX03. The detector was used in ToA mode. The color in each pixel represents the time-stamp of each interaction with respect to the end of the frame exposure time; (c) Same as Fig. 5.4a but for TPX07 with frame exposure time of 0.5 s; (d) Same as Fig. 5.4a but for TPX09 with a frame exposure time of 1 s.
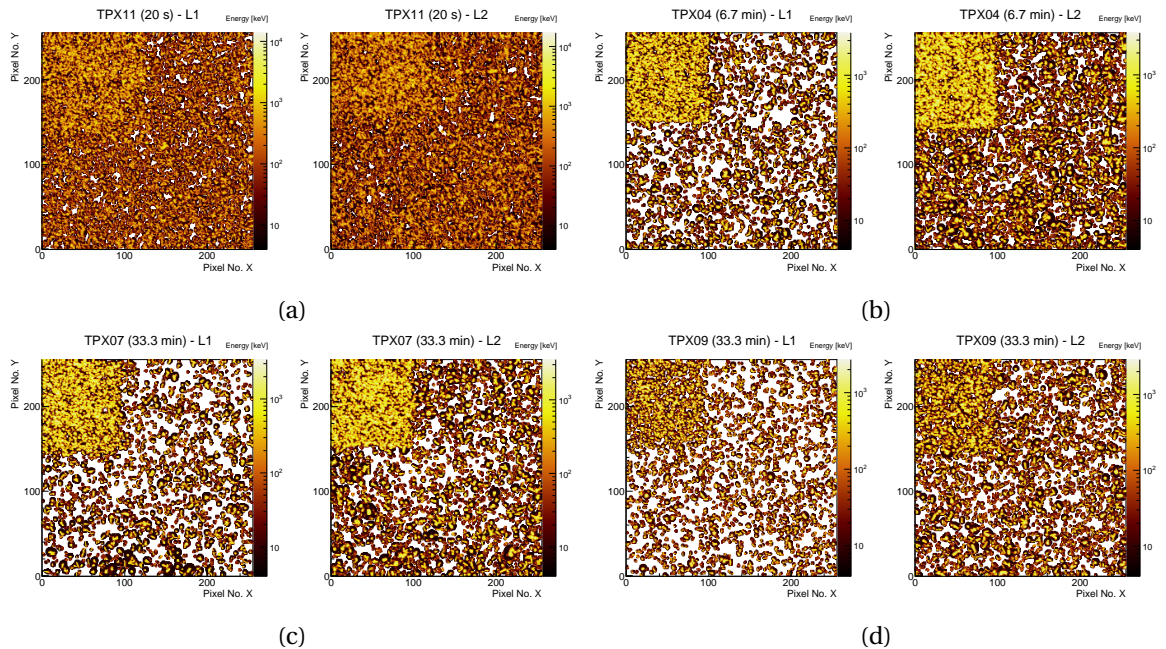
Figure 5.5: Integral frames of the HETE signal measured by different detectors. The ^{6}LiF-region shows an enhancement in the presented devices. The contrast is greater for the thin layers (layer 1) and for detectors with lower contribution of fast neutron interactions.
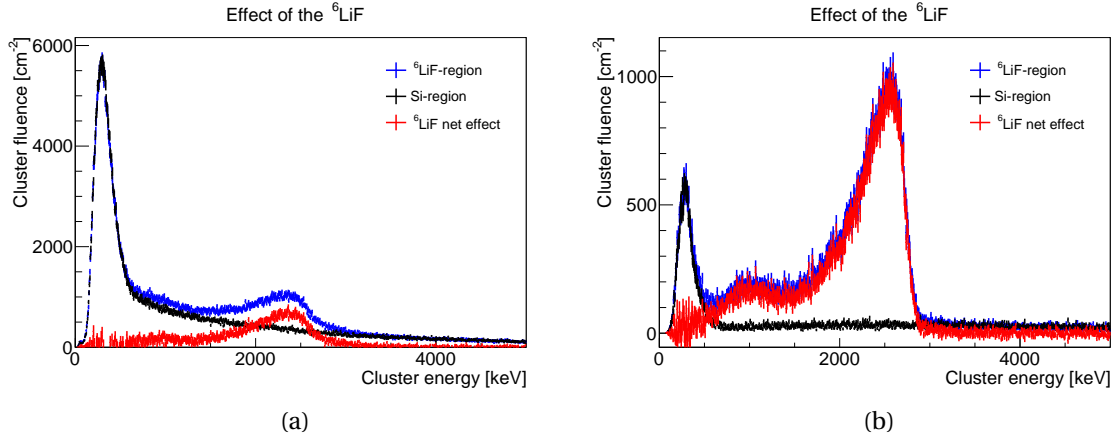
Figure 5.6: Demonstration of the effect of the ^{6}LiF converter: Subtracting the HETE energy deposition spectra in the uncovered (black) from the ^{6}LiF-region (red), scaled according to the converter areas, the typical energy deposition spectrum of the α and the ^{3}H after thermal neutron conversion remains. The data was taken on May 31, 2016 with TPX01. The effective live time of the device was 164 s; (b) Same as Fig 5.6a, but for TPX07. The effective live time of the device was 9.5 hours.

charge collection efficiency by investigating the position of the high energy edge as a function of total ionizing doses (TID). Additional information can be gained by an analysis of the TID dependent changes of the cluster morphology.

At device i, the thermal neutron fluxes are calculated as the average of both layers, according to:

$$\langle \frac{d\Phi}{dt} \rangle_i = \frac{1}{2} \Sigma_{j=1}^2 \left(\frac{N_{\text{HETE},i,j} - \frac{A_{\text{LiF}}}{A_{\text{Si}}} N_{\text{HETE},i,j}}{A_{\text{LiF}} \times t_{\text{meas.}} \times \epsilon_{\text{th.},i,j}} \right),$$ (5.1)

where $\epsilon_{\text{th.},i,j}$ denotes the calibrated efficiencies of device i and layer j. The results are shown as a function of time for each device in Fig. 5.7. Figure 5.8 shows the neutron fluxes at the different devices per unit luminosity, which was determined by:

$$\frac{\Phi}{\mathscr{L}} = \frac{\langle \frac{d\Phi}{dt} \rangle \times (t_{\text{end}} - t_{\text{start}})}{\int_{t_{\text{start}}}^{t_{\text{end}}} \mathscr{L}(t)},$$ (5.2)

with the average neutron flux during the fill $\langle \frac{d\Phi}{dt} \rangle$ and the start and end times of the fill t_{start} and t_{end}, respectively.

TPX02 and TPX12 are dedicated to a precision measurement of luminosity [SAA$^+$15]. They measure overexposed frames, in which individual clusters can no longer be separated. Thus, these devices cannot be used for the measurement of the thermal neutron fluxes.

As the thermal neutrons are only visible during collision periods, their signal is a clear indicator for beam-beam interactions. It is an independent measurement for the validation of the results of the luminosity measurements, whereby systematic uncertainties from degradation of the detectors due to radiation damage and systematic effects arising from the activation in the surrounding material [SAA$^+$15], do have a minor effect. However, owing to low statistics, an independent measurement of luminosity with the thermal neutron signal could lack precision. A comprehensive study of the measured neutron signal including also fast neutrons will be the subject of further investigations and can be an important input into ATLAS simulation verifications.
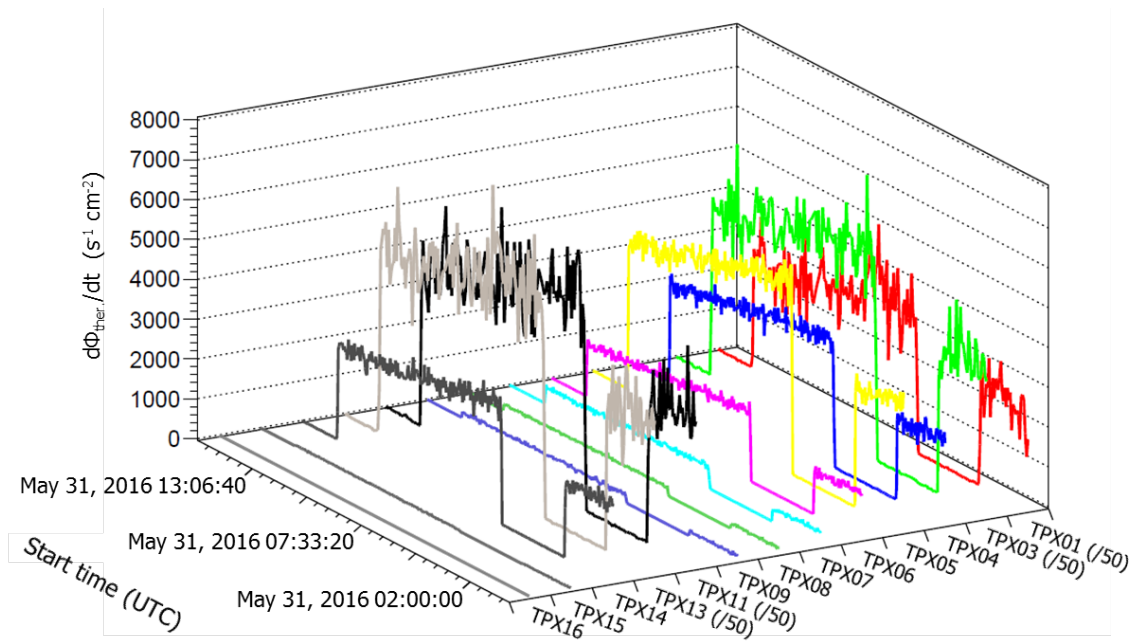
Figure 5.7: Thermal neutron fluxes as measured by the different devices during LHC Fill 4965 on May 31, 2016.
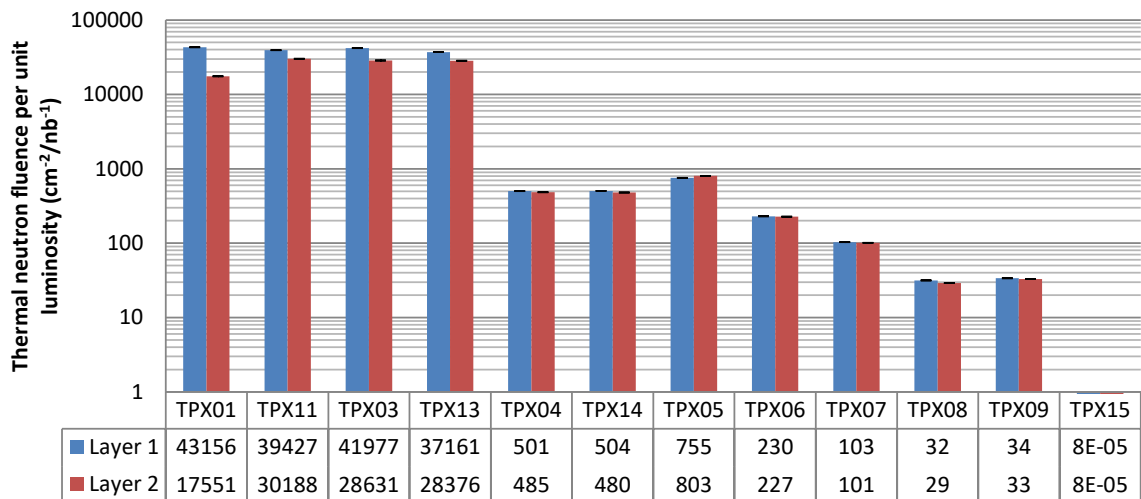

Figure 5.8: Thermal neutron fluxes per unit luminosity for the different TPX devices as measured during LHC Fill 4965 on May 31, 2016 (accumulated luminosity: $170{,}640 \, \text{nb}^{-1}$).

6 | Non-ionizing energy losses and radiation damage studies

At the end of a particle trajectory, the non-ionizing energy losses (NIEL) become increasingly important and begin to compete with the ionizing energy losses (IEL). The proportion of IEL and NIEL to the particle's energy loss is given by the partition function, whose experimental determination is described for recoil silicon atoms stopped in a silicon layer in Sec. 6.2. Section 6.1 illustrates the importance of knowledge of the partition function for radiation damage estimation. The understanding of radiation damage is of major interest not only for the vertex detectors in the big experiments at the LHC (ATLAS, CMS, LHCb), but also to guarantee safe use of electronics in aviation, space applications, and at nuclear power plants. The following discussion focuses on silicon and only gives a brief overview of the aspects of radiation damage. The interested reader might refer to the comprehensive works [Mol99] and [LR07].

6.1 Background

6.1.1 Displacement damage

Whereas IEL are due to collisions with atomic electrons, NIEL are due to collisions with the atoms of the lattice, leading to lattice vibrations (phonons), or the displacement of atoms from their lattice sites. In the latter case, a vacancy (V) and an atom in an interstitial (I) position are left behind: A configuration known as Frenkel pair [LR07]. The energy required to form a stable defect E_{d} (displacement energy) in silicon is 13 eV-33 eV, whereby the exact value depends on the displaced atom's direction of motion [LR07]. If the energy transfer to the initially displaced atom (primary knock-on atom, PKA) is high enough, it can displace atoms from their lattice sites, which again can displace atoms, and so on. Thus, a cascade of displacements occurs, creating a region with a high local density of defects (cluster of defects).

In contrast to electrons or γ-rays, which typically create single Frenkel pairs (point defects), ions (or recoil nuclei after neutron impact) create clusters of defects [SMM03, Lin03]. As an example, the simulated distribution of defects created by a 50 keV silicon atom is shown in Fig. 6.1. With the recoil silion's range of 1000 Å, the defects spread out over a volume of $\approx 600 \times 200 \times 700 \, \text{Å}^3$ [Lin03].

6.1.2 Annealing

The creation of defects is not the end of the story. Interstitials and vacancies are highly mobile at room temperatures, so that they can migrate or diffuse through the sensor layer and either form more stable defects (divacancies, ...) or recombine [Mol99]. The restructuring of defects, and eventually their recombination, is called annealing. It typically implies a reduction of the amount of
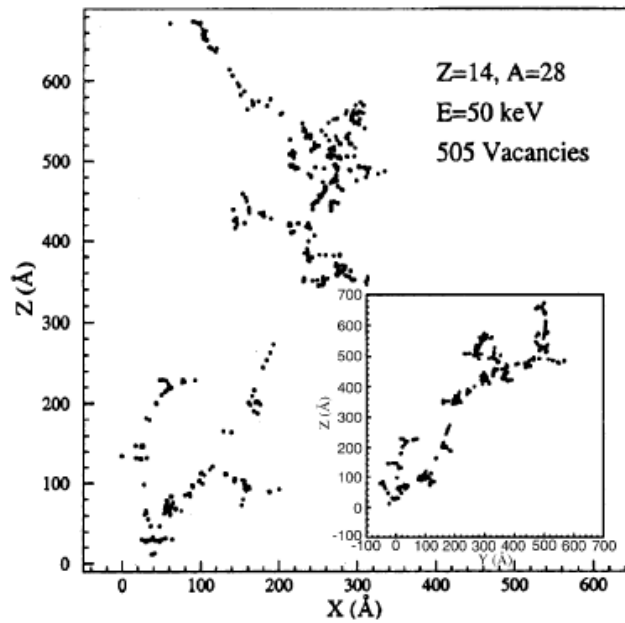
Figure 6.1: Simulated distribution of vacancies created by a 50 keV silicon recoil atom, produced for example by a 1 MeV neutron. From [Lin03].
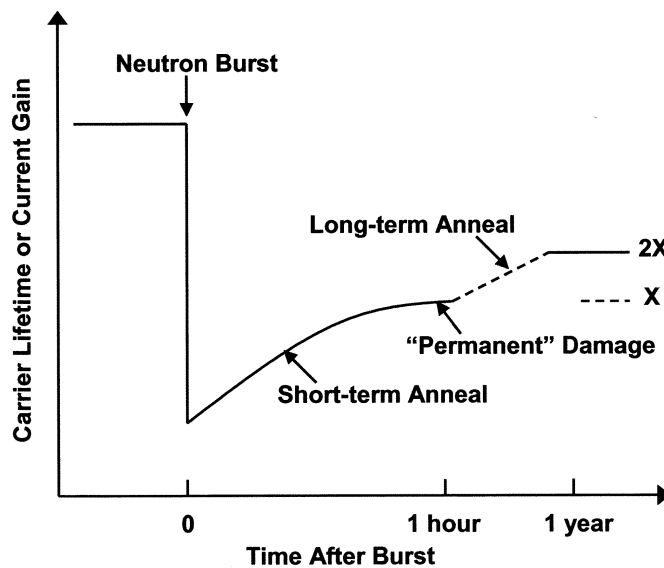
Figure 6.2: Schematic illustration of short-term and long term annealing. From [SMM03].

defects [SMM03]. Increasing the temperature or the injection of charges can be used to enhance annealing.

Annealing processes are further separated into short-term (seconds to minutes) and long term processes. Since the long-term processes can last more than one year for storage at room temperature, the radiation damage situation prevailing at 1 hour after irradiation is used as a measure for the "permanent damage" (see also Fig. 6.2) [SMM03].

The resulting stable defects can alter the properties of the detectors, for example by reducing minority carrier lifetimes, creating charge trapping centers, or degrading the charge carrier mo-
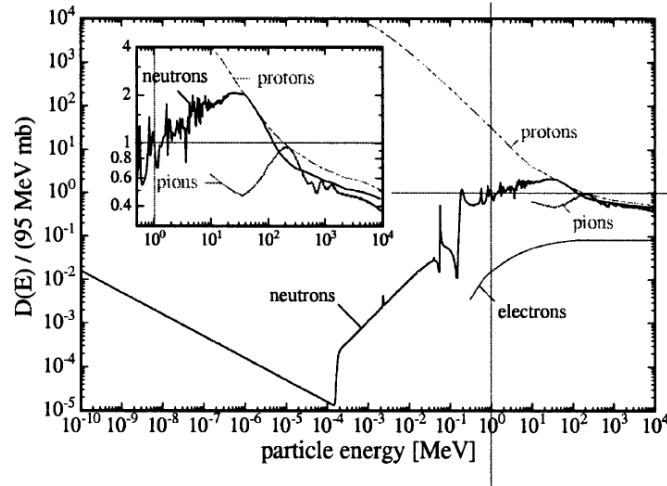
Figure 6.3: Damage function for different particles. From [Lin03].

bilities. From a practical viewpoint, these defects are visible through decreased charge collection efficiency, increased leakage current, and increasing full depletion voltage (reverse bias needed to create a fully depleted sensor volume). These "macroscopic" effects are used to "measure" (assess) the permanent radiation damage introduced to the bulk material.

6.1.3 NIEL scaling hypothesis of bulk damage

Most of the initially created Frenkel pairs recombine (on average 60%, in dense defect regions up to 95% [Mol99]). Still, it was found empirically that the bulk (displacement) damage proportionally increases with increasing NIEL (see [SMM03] and references therein). Therefore, proper knowledge of the amount of IEL and NIEL deposited by ionizing radiation is required for radiation damage assessment. The fraction of NIEL is described by the so-called partition function $P_{\mathrm{NIEL}}(E_{\mathrm{R}})$. The damage function (also called displacement cross-section) is written as [LR07]:

$$D(E) = \Sigma_k \sigma_k(E) \times \int_0^{E_{\mathrm{R}}^{\max}} f_k(E, E_{\mathrm{R}}) P(E_{\mathrm{R}}) dE_{\mathrm{R}}, \tag{6.1}$$

where E_{R} is the energy of the PKA, $f_k(E, E_{\mathrm{R}})$ is the probability for a particle with energy E to produce a PKA with energy $f_k(E, E_{\mathrm{R}})$, and σ_k is the cross-section of reaction k. Hereby, the index k includes all possible interactions between the incoming particle with energy E and atoms in the medium leading to displacement. The damage function is shown for different particles in Fig. 6.3. Neutrons above approximately 185 eV carry enough energy to displace an atom from its lattice site. The rise towards lower energies from there is due to displacements caused by γ-rays arising in neutron capture reactions [Mol99]. The proton damage function is higher than the one for neutrons due to Coulomb interactions.

The energy density E_{dis} deposited through atomic displacements related to a neutron spectral fluence $\Phi(E)$ (neutrons cm^{-2} MeV^{-1}) is the damage energy E_{de} and given by [LR07]:

$$E_{\mathrm{de}} = \frac{\rho N_{\mathrm{A}}}{A} \times \int D(E)\Phi(E) dE [MeV\, cm^{-3}] \tag{6.2}$$

where N_{A} is the Avogadro constant, ρ is the density, and A is the mass number of the medium. From the damage energy, the average number of Frenkel pairs can be estimated by the modified Kinchin-Pease formula [LR07]:

$$N_{\mathrm{FP}} \approx \frac{E_{\mathrm{de}}}{2.5 E_{\mathrm{d}}}. \tag{6.3}$$

45

For a more detailed discussion see the following Sec. 6.2.

6.1.4   Hardness factor

In order to compare the damage caused by different particles, the hardness factor κ was introduced, which relates the damage caused by the spectrum of interest to the damage caused by the irradiation with monoenergetic 1 MeV neutrons $D_n(1\,\text{MeV}) = 95\,\text{MeV mb}$. κ is defined as [Mol99]:

$$\kappa = \frac{\int D(E)\Phi(E)dE}{D_n(1\,\text{MeV}) \times \int \Phi(E)dE}. \tag{6.4}$$

For a given neutron spectrum $\Phi(E)$, the 1 MeV neutron equivalent fluence $\Phi_{\text{eq.}}$ is then obtained by [Mol99]:

$$\Phi_{\text{eq.}} = \kappa \int \Phi(E)dE. \tag{6.5}$$

6.1.5   The partition function: Why do we measure?

The crucial point of the calculation of NIEL and damage function is accurate knowledge of the partition function. The work shown in Sec. 6.2 presents an experimental determination of the partition function for recoil silicon atoms in a silicon lattice. Based on the integral equations derived by Lindhard in 1963 [LNST63], the Norgett-Torrens-Robinson [RT74] equations are used to calculate the ionizing and non-ionizing energy depositions. When compared with the measurement of Sattler performed in 1965 [Sat65], deviations from the theory, in particular at low recoil energies can be found. These were, however, not significant due to the large uncertainties of the measurement.

In 2006, Akkerman and Barak [AB06] reported a new method for the determination of the partition function based on computer simulations showing better agreement with experimental data at low recoil energies. However, due to substantial uncertainties of the data points, Sattler's measurement cannot draw a decisive conclusion on model selection. Currently, the NIEL simulation tool SRIM/TRIM [sri] relies on the Norgett-Torrens-Robinson equations as input, whereas an online NIEL calculator [nie] offers the user the option to select either model.

The aim of the presented work was to provide a data set with higher precision. For the first time, a Timepix3 (with a 300 μm thick silicon sensor layer) was employed in a time-of-flight measurement at the white spectrum neutron beam of the Los Alamos Neutron Science Center (LANSCE) [LS06].

6.2 Publication: Ionizing energy depositions after fast neutron impact in silicon

The following work was published as "Ionizing energy depositions after fast neutron impact in silicon" by B. Bergmann, S. Pospisil, I. Caicedo, J. Kierstead, H. Takai, and E. Frojdh in IEEE Transactions on Nuclear Science, Vol. 63, No.4, 2016. Doi: 10.1109/TNS.2016.2574961

This work demonstrated the successful application of a Timepix3 with a 300 μm sensor layer in a neutron time-of-flight measurement at the pulsed neutron spallation source in the Los Alamos Neutron Science Center. Hereby, the work profited from the improved time resolution and the capability of the Timepix3 to determine the time and the energy deposition simultaneously in each pixel. The results of the work are the following:

- The ionizing energy deposition spectra in the silicon bulk material were shown and interpreted at different neutron impact energies;

- A study of ionizing vs. non-ionizing energy losses of recoil silicon atoms was presented. The results were compared and found to be in agreement with a previous measurement done by Sattler. However, the significance of the presented measurement was increased by better sampling and smaller errors in the relevant energy range;

- The measured partition function (describing the ratio of the ionizing versus the non-ionizing energy losses as a function of silicon recoil energy) was compared to the model predictions of Lindhard and Akkerman-Barak, whereby the data suggests to prefer the latter one.

My own contribution to the work:

- Idea for the measurement;

- Responsibility for the measurement;

- Development if the methodology for the data evaluation;

- Data analysis;

- Interpretation of the physical results;

- Writing of the publication.

Co-authors' contributions:

- Preparation of the beam time proposal;

- Participation at the measurement;

- Detector preparation;

- General discussions.

7 | Improved particle tracking with the Timepix3

An application profiting from the improved capabilities of the Timepix3 was illustrated in the previous chapter. The following application utilizes the improved time resolution and illustrates how it can be used to measure charge carrier drift times, which in turn are used for particle track reconstruction in 3D.

7.1 Background

7.1.1 Particle tracking in High Energy Physics

Particle trackers in the big high energy physics experiments (ATLAS [Col08a] and CMS [Col08b]) are the detection systems closest to the interaction point. They consist of pixel or strip detector planes with different orientations, each measuring particle position. By connecting the points in each layer the particle's trajectory is reconstructed in three dimensions. In order to have a full solid angle coverage such systems have to cover a big area. Currently, the largest track detector is the CMS Inner Tracker, which consists of $\approx 200\,\mathrm{m}^2$ of silicon strip and $1\,\mathrm{m}^2$ of pixel detectors. On the other hand, the trackers should be kept thin, in order to not alter the particle energy or direction significantly.

A space application of such a tracking system can be found in the AMS experiment [Bur02], attached to the ISS, searching for dark matter and antimatter. However, when putting such detection system into space, there are requirements of power consumption and sizes to be met.

Another approach for 3D particle trajectory reconstruction is used in the ALICE experiment [col14], where the inner track detectors are surrounded by a time-projection chamber (TPC). The TPC uses a 2D grid together with the drift times of electrons in a gas volume to determine spatial coordinates. Additionally, the energy released in the gas ($-dE/dx$) is measured.

7.1.2 Particle tracking with Timepix detectors

Ever since it was noted that the Medipix2 detector can be regarded as an active nuclear emulsion [PSE+11, VJHP06], attempts have been made to reconstruct the particle trajectory (mainly the impact angle) and determine its $-dE/dx$ with Medipix2 and its successor Timepix. In contrast to the high energy physics experiments described, where the main goal is precision, Timepix detectors have been in use for particle tracking in places where available space is limited, or situations where weight and power consumption matters. Prominent applications include the measurement of the directions of particles trapped in the Van-Allen belts with the SATRAM device [GPV+16, GBG+16], and the radiation monitoring and dose estimation on the ISS [TPJ+11b, SPK+15]. Timepix "trackers" relying only on a single layer come with some disadvantages:

- The exact orientation of the track cannot be determined. It cannot be said which end was up and which end was down[1];

- The track length and the angle can only be determined from the impact and exit point, giving rather large uncertainties of trajectory reconstruction and $-dE/dx$ determination.

Therefore, to improve the track reconstruction, multilayer approaches were used, for example for the application in particle therapy [JGH$^+$11] and in a Timepix particle tracking telescope [ARvB$^+$13]. However, these telescope setups have the drawback of reduced angular acceptance (field of view). The following work illustrates how the tracking performance of a single layer Timepix3 can be improved by utilizing the charge carrier drift time information to obtain the z-coordinate.

---

[1] By using the charge sharing information this is possible for tracks characterized by a high energy deposition in the sensor layer.

7.2 Publication: 3D track reconstruction capability of a silicon hybrid active pixel detector

The following article was published as "3D track reconstruction capability of a silicon hybrid active pixel detector" by B. Bergmann, M. Pichotka, S. Pospisil, J. Vycpalek, P. Burian, P. Broulim, and J. Jakubek in the European Physical Journal C, Vol. 77, 2017. Doi: 10.1140/epjc/s1

A 500 μm thick silicon sensor layer bump-bonded to the Timepix3 ASIC was used to investigate the improvements for the track reconstruction of particle tracks. Therefore, a measurement was performed in a 120 GeV/c beam at the Super-proton-synchrotron at CERN. The following points are addressed in the work:

- Calibration methods of Timepix3 are outlined and an experimental method for time-walk correction was described;

- A drift time model for charge carriers motion (holes) through a silicon sensor layer was derived and compared to measured data;

- Based on the drift time model, z-coordinates of particle tracks were reconstructed. The z-resolution was determined as a function of interaction depths from measured data. It was shown that a z-resolution of approximately 50 μm can be achieved creating a 3D sensitive volume with a voxel size of $55 \times 55 \times 50\ \mu\text{m}^3$;

- 3D reconstructed charged pions and associated δ-rays were shown. A 3D reconstructed muon track was fitted to demonstrate that the 3D resolution σ_{xyz} is around 60 μm.

My own contribution to the work:

- Idea for the measurement;

- Detector preparation and calibration;

- Development of the methodology for the data evaluation;

- Data analysis;

- Interpretation of the physical results;

- Writing of the publication.

Co-authors' contributions:

- Performing the measurements;

- Design and development of the readout electronics;

- Contribution to detector preparation and calibration;

- General discussions.

Conclusion

Detectors of the Medipix/Timepix family are hybrid pixel detectors developed by the Medipix collaboration(s) hosted at CERN. They consist of a sensor layer divided into a square matrix of 65,536 pixels with a pixel pitch of $55\,\mu$m. In each of the pixels, the number of interactions, the deposited energy, and/or the time of arrival can be measured. In the presented thesis, the capabilities of Timepix and Timepix3 were evaluated for different applications profiting from the pixelation and/or the time-resolution. A dedicated methodology was developed for detector use in specific physics experiments.

In the first experiment, two synchronized Timepix detectors were placed on both sides of a point-like ^{55}Fe source, determining the probability of the rare production of a double K-shell vacancy P_{KK} after the electron capture decay of ^{55}Fe to ^{55}Mn. P_{KK} for ^{55}Fe has already been measured by different approaches, but the precision of the measurements was not high enough for proper theoretical model selection. Additionally, when comparing the ^{55}Fe value with P_{KK}-measurements of the neighboring electron capture isotopes ^{54}Mn and ^{65}Zn, a discrepancy from the Primakoff-Porter scaling was reported. In the presented work, P_{KK} was found to to be $P_{KK} = (1.388 \pm 0.037) \times 10^{-4}$, with a systematic uncertainty of $\Delta P_{KK,syst} = 0.042 \times 10^{-4}$, which exceeds the precision of all previous measurements. This result is consistent on a $1.5\,\sigma$ level with the values reported for ^{54}Mn assuming Primakoff-Porter scaling, but it also confirms the discrepancy with ^{65}Zn (values presented in other works had to be corrected for the differing fluorescence yields in the single and double vacancy states). Thus, further investigations are strongly encouraged, such as a triple coincidence experiment to eliminate the impact of the γ-ray from the relaxation of the ^{65}Zn.

When compared with theoretical values, the presented result was not consistent with any of the proposed model calculations for P_{KK} prediction.

Thanks to the pixelation of the detectors, the angular correlation between the hypersatellite and satellite photons emitted during the relaxation of the double vacancy state could be extracted for the first time. The experimentally determined anisotropy parameter $\beta_2^{\mathrm{exp}} = 0.097 \pm 0.053$ is in good agreement with $\beta_2^{\mathrm{theo.}} = 0.097 \pm 0.053$ obtained in the electric-dipole approximation.

The presented measurements and evaluation techniques had to cope with a considerable amount of detector dead time and the fact that only crude energy information (cluster size and threshold) was available. Using the newly developed Timepix3 detectors for such investigations, measurement time and systematic error could be significantly reduced due to a data-driven readout scheme and the possibility to measure energy and time simultaneously.

The second use of Timepix type detectors for particle physics experiments was based on their adaptation for the detection of neutrons. Neutron converter materials were attached to the Timepix segmenting the Timepix into areas with higher detection efficiencies for neutrons of different energies. Proper selection of neutron converters together with a pattern recognition algorithm provided good separation of the neutron field from γ-rays. Neutron detection efficiencies were measured and compared to simulations.

The probability of detecting thermal neutrons through the ^{6}Li(n,α)^{3}H-reaction (in an $\approx 1.6\,\mathrm{mg/cm^2}$ thick ^{6}LiF-layer) was found to be $\approx 0.5\%$. Fast neutrons with energies above 1 MeV were detected through recoil protons from a 1.2 mm thick CH$_2$ (polyethylene, PE) layer. Fast neutron interactions in the silicon sensor layer were estimated in an uncovered region and subtracted. The time-of-flight technique was used to study the energy dependence of the PE converter regions' detection efficiencies to fast neutrons in the energy range from few hundreds of keV up to 600 MeV. A maximal efficiency of approximately 0.032% was found around 16 MeV. By adding an aluminum foil of $\approx 100\,\mu$m thickness below a part of the PE, a region with differing fast neutron response was created, which can be used together with the response below the PE layer to assess the hardness of the neutron spectrum.

To increase the capability of separating neutrons from charged particles and to estimate the directionality of the fast neutron component, a two-layer approach was introduced. The data analysis and the performance of the device were illustrated by data evaluation in typical mixed radiation fields: in a particle therapy application, for radiation monitoring at a beam line, and by the determination of thermal neutron fluxes at 16 positions in the ATLAS experiment. The presented results of the ATLAS-TPX devices inside ATLAS are a valuable input for benchmarking simulations, which are used to estimate radiation doses and particle fluxes at the different ATLAS subdetector systems. It is also used for monitoring the stability of the ATLAS luminosity measurement.

In the third application, a Timepix3 detector was employed for a time-of-flight experiment in a fast neutron beam with the goal of improving the understanding of neutron interactions and the corresponding energy depositions in silicon. It was motivated by the needs of radiation damage assessment. With the capability of the Timepix3 to detect the energy and time simultaneously in each pixel, the energy deposition spectra of fast neutrons in a 300 μm thick silicon sensor layer were recorded. By spectrum interpretation, the energy depositions of recoil silicon after neutron elastic scattering were separated from inelastic interactions so that the competition of ionizing (IEL) vs. non-ionizing energy losses (NIEL) could be studied in the neutron energy range from 200 keV - 10 MeV. The obtained partition function is in agreement with a previous measurement by Sattler and was compared with two theoretical models: the model of Norgett-Torrens and Robinson, which is based on the Lindhard equations and standardly used in NIEL simulation tools (such as SRIM), and the newer model of Akkerman and Barak. The presented data underlines the trend to prefer the Akkerman and Barak model, especially at low recoil silicon energies (down to $T_{\mathrm{Si}} \approx 20\,$keV).

The last part covered a methodological development for future applications of the Timepix3 for advanced particle tracking in physics experiments. It discusses the Timepix3's capabilities to perform 3D reconstructions of particle trajectories in a 500 μm thick silicon sensor layer. Therefore, a similar technique to that of a time-projection chamber (TPC) was used. The 3D coordinates of particle tracks could be obtained in a silicon semiconductor device, thus profiting from all the advantages of solid state detectors (small dimensions, speed of operation, and high stopping power) compared to the gas-filled TPC. With the improved time resolution of the Timepix3, it was possible to determine the drift time of created charge carriers with a precision of 1.5625 ns. The presented study investigated the achievable z-resolutions for different bias voltages and discussed the effect of an inaccurate drift time model. It was shown that a z-resolution of 50 μm can be achieved (with a bias of 130 V applied to a 500 μm thick silicon sensor), which could be reduced to 28.5 μm with an improved description of the drift time dependence on interaction depth. Timepix3 can thus be seen as a 3D detector with $55 \times 55 \times 50\,\mu\mathrm{m}^3$ voxel size. The 3D paths of 120 GeV/c pion tracks and associated δ-rays through the 500 μm thick silicon sensor layer were illustrated.

Zusammenfassung

Detektoren der Medipix/Timepix Familie sind hybride Pixeldetektoren, die am CERN im Rahmen der Medipix Kollaborationen entwickelt wurden. Medipix/Timepix Detektoren besitzen ein aktives Detektionsvolumen (den sogenannten Sensor), dessen Fläche in eine quadratische Matrix aus 65.536 (256 x 256) Pixel unterteilt ist. Die Kantenlänge eines Pixels beträgt 55 μm. In jedem Pixel kann entweder die Anzahl eintreffender ionisierender Teilchen, die im Pixel deponierte Energie und/oder der Zeitpunkt einer Wechselwirkung gemessen werden. In der vorliegenden Arbeit wird das Potenzial von Timepix und Timepix3 Detektoren in Anwendungen untersucht, die von der Pixelierung und/oder der Zeitauflösung profitieren. Für jedes der beschriebenen Experimente wurde eine spezielle Auswertemethodik entwickelt.

Im ersten Experiment wurden zwei synchronisierte Timepix Detektoren auf beiden Seiten einer punktförmigen ^{55}Fe-Quelle angebracht, mit dem Ziel die Wahrscheinlichkeit der Erzeugung einer doppelten K-Schalen Leerstelle P_{KK} für ^{55}Fe zu bestimmen. Hierbei zerfällt ^{55}Fe in der Elektroneneinfangreaktion zu ^{54}Mn. P_{KK} wurde für ^{55}Fe bereits mehrfach, mit verschiedenen experimentellen Anordnungen, gemessen. Die Präzision reichte bisher aber nicht aus, um ein bestimmtes theoretisches Modell zu favorisieren. Desweiteren gibt es eine auffällige Dikrepanz beim Vergleich der P_{KK}-Werte von ^{55}Fe und den benachbarten Elektroneneinfangsisotopen ^{54}Mn und ^{65}Zn, wenn man die Primakoff-Porter Skalierung zu Grunde legt. Die vorliegende Arbeit bestimmt $P_{KK} = (1.388 \pm 0.037) \times 10^4$, wobei die systematische Messunsicherheit als $\Delta P_{KK,syst} = 0.042 \times 10^{-4}$ angegeben werden kann. Dies ist bis heute das Ergebnis mit der höchsten Genauigkeit. Extrapoliert man das Ergebnis unter Annahme der Primakoff-Porter Skalierung, ergibt sich eine Übereinstimmung mit den am ^{54}Mn gemessen Werten auf einem $1.5\,\sigma$-Level. Die Abweichung für das Isotop ^{65}Zn bleibt allerdings bestehen. Die Werte aus anderen Publikationen wurden hierbei korrigiert um die unterschiedlichen Floureszenzausbeuten für die Erzeugung einer doppelten oder einfachen Leerstelle in der K-Schale zu berücksichtigen. Das Ergebnis konnte nicht in Einklang gebracht werden mit theoretischen Modellvorhersagen, sodass eine sorgfältige Überprüfung dieser Modelle, und der bei der Berechnung gemachten Anmahmen, angeraten wird.

Mit der Pixelierung der verwendeten Detektoren konnte gleichzeitig die Winkelverteilung zwischen den emittierten Hypersatelliten und Satellitenphotonen bestimmt werden. Hierbei fand sich ein Anisotropieparameter $\beta_2^{exp} = 0.097 \pm 0.053$. Dieser stimmt mit dem Wert $\beta_2^{theo.} = 0.097 \pm 0.053$, berechnet in elektrischer Dipol Näherung, gut überein.

Die wesentlichen Schwachstellen der benuzten Detektortechnologie waren der hohe Anteil an Totzeit und die Tatsache, dass die Energie der wechselwirkenden Quanten nur unpräzise (durch die Clustergröße und die Detektorschwelle) abgeschätzt werden konnte. Mit einer neuentwickelten Detektortechnologie, dem Timepix3, welcher Daten in Echtzeit und mit vernachlässigbarer Totzeit, auslesen kann und in jedem Pixel sowohl Energie als auch Zeit misst, können sowohl die Messzeit als auch der systematische Fehler reduziert werden.

Die zweite vorgestellte Anwendung des Timepix Detektors im Bereich der Teilchenphysik ist

dessen Adaption zum Nachweis von Neutronen und deren Unterscheidung von geladenen Teilchen und γ-Strahlen. Dazu wurden verschiedene Konversionsmaterialien auf einem Timepix Detektor angebracht, durch welche Neutronen in geladene Teilchen mit vergleichsweise hoher Energiedeposition im Siliziumsensor umgewandelt werden. Durch die Wahl geeigneter Neutronenkonverter und einer Pattern Recognition Software konnte eine gute Separation von Neutronen und Photonen erreicht werden.

Die Nachweiswahrscheinlichkeit thermischer Neutronen durch die ^{6}Li(n,α)^{3}H-Reaktion (in einer $\approx 1.3\,\mathrm{mg/cm^2}$ dicken ^{6}LiF-Schicht) konnte mit $\approx 0.5\%$ angegeben werden. Schnelle Neutronen mit Energien über 1 MeV werden durch rückgestreute Protonen aus einer 1,2 mm dicken CH_2 (Polyethylen, PE)-Schicht nachgewiesen. Das Signal, das von Wechselwirkungen der Neutronen im Silizium des Sensors erzeugt wird, wird im einem unbedeckten Teil des Sensor gemessen und abgezogen. Mit Hilfe der Neutronenflugzeitmessung konnte die Energieabhängigkeit der Nachweiswahrscheinlichkeit schneller Neutronen bis 600 MeV bestimmt werden. Die maximale Nachweiswahrscheinlichkeit von 0.032 % findet man bei 16 MeV. Durch Einbringen einer dünnen, $\approx 100\,\mu m$ dicken, Aluminiumfolie zwischen der einen Hälfte des PE-Blocks und dem Sensor, wird eine Region mit abweichender Energieantwort erzeugt, welche durch Vergleich mit der PE-Region dazu benutzt werden kann die Energie des Neutronenfeldes zu bestimmen.

Um die Fähigkeit des Detektors zur Unterscheidung von Neutronen und geladenen Teilchen zu erhöhen und um die dominierende Richtung der schnellen Neutronen zu bestimmen, wurde ein 2-lagiger Detektionsaufbau benutzt. Die Methodik der Datenanalyse und die Performance des Detektionsaufbaus wurden anhand der Auswertung in typischen gemischten Strahlungsfeldern veranschaulicht. Als Beispiele dienten die Strahlentherapie, die Messung der Strahlungslevel an einem Teilchenstrahl und die Bestimmung der thermischen Neutronenflüsse an 16 unterschiedlichen Positionen innerhalb des ATLAS Experiments am CERN. Die hier gewonnenen Ergebnisse stehen als wertvolle Vergleichsdaten zum Benchmarking von Simulationen, die dazu verwendet werden Strahlungsdosen und Teilchenflüsse in den verschiedenen Unterdetektoren abzuschätzen, zur Verfügung. Die thermischen Neutronenflüsse werden außerdem benutzt um die Stabilität der Luminositätsmessung zu überprüfen.

In der dritten Anwendung werden mit einem Timepix3 Detektor Neutronenflugzeiten gemessen um die Wechselwirkung und die Energiedeposition von Neutronen im Silizium näher zu untersuchen. Die Ergebnisse wurden im Kontext der Strahlenschäden diskutiert. Durch gleichzeitige Messung der Energiedeposition und der Ankunftszeit, konnten den Energiedepositionen in dem $300\,\mu m$ dicken Siliziumsensor die zugrunde liegenden Neutronenenergien zugeordnet werden. Durch Analyse der gemessenen Spektren wurden die Energiedepositionen der Neutronenstreuung von inelastischen Prozessen getrennt und der Anteil von nichtionisierenden und ionisierenden Energieverlusten rückgestreuter Siliziumatome für Neutronenenergien im Bereich 200 keV bis 10 MeV ermittelt. Die dabei gewonnenen Partitionsfunktionen sind im Einklang mit einer früheren Messung von Sattler und wurden verglichen mit zwei theoretischen Modellen: Dem Modell von Norgett, Torrens und Robinson, welches auf den Lindhard Gleichungen basiert und als Standard für NIEL Berechnungen verwendet wird (zum Beispiel in SRIM), und einem neueren Modell von Akkerman und Barak. Die gemessen Daten bestätigen den Trend, das Modell von Akkerman und Barak zu bevorzugen, insbesondere für niedrigere Energien der rückgestreuten Siliziumatome (bis $T_{Si} \approx 20\,\mathrm{keV}$).

Der letzte Teil der Arbeit beschreibt eine Weiterentwicklung der Methodik für die Anwendung von Timepix3 Detektoren zur verbesserten Vermessung von Teilchentrajektorien. Es wird untersucht, inwieweit ein Timepix3 dazu verwendet werden kann 3-dimensionale Teilchentrajektorien in einem $500\,\mu m$ dicken Silizium Sensor zu rekonstruieren. Dabei wurde eine ähnliche Methodik

wie in Spurendriftkammern (Time-Projection-Chamber, TPC) verwendet. Da die Teilchenspuren in einem Halbleiterdetektor rekonstruiert wurden, profitiert man von dessen Vorteilen gegenüber Gasdetektoren (kleineres Volumen, hohe Geschwindigkeit, hohe Stopping Power).

Mit der verbesserten Zeitauflösung des Timepix3, konnte die Driftzeit der erzeugten freien Ladungsträger mit einer Präzision von 1.5625 ns gemessen werden. In der vorliegenden Arbeit wiurde die aufgrund dieser Zeitauflösing erreichbare $z-$Auflösung untersucht. Hierbei wird die Auswirkung eines fehlerbehafteten Driftzeitmodells als systematischer Fehler einbezogen. Es konnte eine $z-$Auflösung von 50 μm erreicht werden (bei einer anliegenden Biasspannung von 130 V über einem 500 μm dicken Silizium Sensor). Durch Verbesserung des Driftzeitmodell könnte eine $z-$Auflösung von 28.5 μm erreicht werden. Mit der beschriebenen Methodik konnte somit ein 3D-Detektor mit einer Voxelgröße von $55 \times 55 \times 50$ μm^3 erzeugt werden. Zur Versanschaulichung wurden 3D-Visualisierungen von Pionenspuren, auf ihrem Weg durch den 500 μm dicken Sensor, und die zugehörigen δ-Elektronen dargestellt.

Bibliography

[AB06]   A. Akkerman and J. Barak. New Partition Factor Calculations for Evaluating the Damage of Low Energy Ions in Silicon. *IEEE Transactions on Nuclear Science*, 53(6):3667–3674, Dec 2006.

[abs]   Attenuation Coefficients. `http://www.nuclear-power.net/nuclear-power/reactor-physics/interaction-radiation-matter/interaction-gamma-radiation-matter/gamma-ray-attenuation/linear-attenuation-coefficient/`. Accessed on 30.10.2017.

[act]   Neutron Activation Foils. `http://www.shieldwerx.com/activation-foils.html`. Accessed on 30.10.2017.

[And33]   C. D. Anderson. The Positive Electron. *Phys. Rev.*, 43:491–494, Mar 1933.

[ARvB$^+$13] K. Akiba, P. Ronning, M. van Beuzekom, V. van Beveren, S. Borghi, H. Boterenbrood, J. Buytaert, P. Collins, A. Dosil Suarez, R. Dumps, L. Eklund, D. Esperante, A. Gallas, H. Gordon, B. van der Heijden, C. Hombach, D. Hynds, M. John, A. Leflat, Y. Li, I. Longstaff, A. Morton, N. Nakatsuka, A. Nomerotski, C. Parkes, E. Perez Trigo, R. Plackett, M. M. Reid, P. Rodriguez Perez, H. Schindler, T. Szumlak, P. Tsopelas, C. Vazquez Sierra, J. Velthuis, and M. Wysokinski. The Timepix Telescope for high performance particle tracking. *Nuclear Instruments and Methods in Physics Research Section A: Accelerators, Spectrometers, Detectors and Associated Equipment*, 723(Supplement C):47 – 54, 2013.

[BBJ$^+$17] P. Burian, P. Broulim, M. Jara, V. Georgiev, and B. Bergmann. Katherine: Ethernet Embedded Readout Interface for Timepix3. *Journal of Instrumentation*, 12(11):C11001, 2017.

[BCD$^+$10] M.-M. Bé, V. Chisté, C. Dulieu, E. Browne, C. Baglin, V. Chechev, N. Kuzmenco, R. Helmer, F. Kondev, D. MacMahon, and K. B. Lee. Table de Radionuclides (Comments on evaluation). 2010.

[BCJ$^+$74] J. P. Briand, P. Chevalier, A. Johnson, J. P. Rozet, M. Tavemier, and A. Touati. Experimental determination of the energy of K hypersatellite lines for various elements. *Physics Letters A*, 49:51–53, Aug 1974.

[BCL07]   M. Bigas, E. Cabruja, and M. Lozano. Bonding techniques for hybrid active pixel sensors (HAPS). *Nuclear Instruments and Methods in Physics Research Section A: Accelerators, Spectrometers, Detectors and Associated Equipment*, 574(2):392 – 400, 2007.

[BCL17]   R. Ballabriga, M. Campbell, and X. Llopart. Asic developments for radiation imaging applications: The medipix and timepix family. *Nuclear Instruments and Methods*

in Physics Research Section A: Accelerators, Spectrometers, Detectors and Associated Equipment, 2017.

[BCTR71]   J. P. Briand, P. Chevallier, M. Tavernier, and J. P. Rozet. Observation of K hypersatellites and KL satellites in the X-Ray Spectrum of Doubly K-Ionized Gallium. *Phys. Rev. Lett.*, 27:777–779, Sep 1971.

[BEB60]   R. L. Bramblett, R. I. Ewing, and T. W. Bonner. A new type of neutron spectrometer. *Nuclear Instruments and Methods*, 9(1):1 – 12, 1960.

[Bet30]   H. Bethe. Zur Theorie des Durchgangs schneller Korpuskularstrahlen durch Materie. *Annalen der Physik*, 397(3):325–400, 1930.

[Bic88]   H. Bichsel. Straggling in thin silicon detectors. *Rev. Mod. Phys.*, 60:663–699, Jul 1988.

[Blo33]   F. Bloch. Zur Bremsung rasch bewegter Teilchen beim Durchgang durch Materie. *Annalen der Physik*, 408(3):285–320, 1933.

[Boh87]   III. On the Theory of the Decrease of Velocity of Moving Electrified Particles on Passing Through Matter: Phil. Mag. 25 (1913) 10–31. In J. Thorsen, editor, *The Penetration of Charged Particles through Matter (1912–1954)*, volume 8 of *Niels Bohr Collected Works*, pages 47 – 71. Elsevier, 1987.

[bss]   Bonner Spheres Spectrometer. `http://www.elsenuclear.com/en/bonner-spheres-spectrometer`. Accessed on 30.10.2017.

[bub]   Bubble Detectors. `http://www.asc-csa.gc.ca/eng/sciences/osm/detector.asp`. Accessed on 30.10.2017.

[Bur02]   W. J. Burger. The AMS silicon tracker. *Nuclear Physics B - Proceedings Supplements*, 113(1):139 – 146, 2002.

[BvBJ⁺03]   D. San Segundo Bello, M. van Beuzekom, P. Jansweijer, H. Verkooijen, and J. Visschers. An interface board for the control and data acquisition of the Medipix2 chip. *Nuclear Instruments and Methods in Physics Research Section A: Accelerators, Spectrometers, Detectors and Associated Equipment*, 509(1):164 – 170, 2003. Proceedings of the 4th Internatonal Workshop on Radiation Imaging Detectors.

[CBB⁺68]   G. Charpak, R. Bouclier, T. Bressani, J. Favier, and C. Zupancic. The use of multiwire proportional counters to select and localize charged particles. *Nuclear Instruments and Methods*, 62(3):262 – 268, 1968.

[Cha53]   G. Charpak. *Comptes Rendus*, 237:243, 1953.

[Che91]   M. H. Chen. Auger transition rates and fluorescence yields for the double-K-hole state. *Phys. Rev. A*, 44:239–242, Jul 1991.

[CHL⁺13]   M. Campbell, E. Heijne, C. Leroy, J.-P. Martin, G. Mornacchi, M. Nessi, S. Pospisil, J. Solc, P. Soueid, M. Suk, D. Turecek, and Z. Vykydal. Analysis of the Radiation Field in ATLAS Using 2008 2011 Data from the ATLAS-MPX Network. Technical Report ATL-GEN-PUB-2013-001, CERN, Geneva, Apr 2013.

[CMT91]   J. L. Campbell, J. A. Maxwell, and W. J. Teesdale. Double K-shell ionization in the electron capture decay of ^{55}Fe. *Phys. Rev. C*, 43:1656–1663, Apr 1991.

[Col08a]   The ATLAS Collaboration. The ATLAS Experiment at the CERN Large Hadron Collider. *Journal of Instrumentation*, 3(08):S08003, 2008.

[Col08b]   The CMS Collaboration. The CMS experiment at the CERN LHC. *Journal of Instrumentation*, 3(08):S08004, 2008.

[col14]   ALICE collaboration. Performance of the ALICE experiment at the CERN LHC. *International Journal of Modern Physics A*, 29(24):1430044, 2014.

[DBB+10]   A. Donzella, M. Barbui, F. Bocci, G. Bonomi, M. Cinausero, D. Fabris, A. Fontana, E. Giroletti, M. Lunardon, S. Moretto, G. Nebbia, M.M. Necchi, S. Pesente, G. Prete, V. Rizzi, G. Viesti, and A. Zenoni. A proton recoil telescope for neutron spectroscopy. *Nuclear Instruments and Methods in Physics Research Section A: Accelerators, Spectrometers, Detectors and Associated Equipment*, 613(1):58 – 64, 2010.

[Dem17]   W. Demtröder. *Experimentelle Techniken und Geräte in Kern- und Hochenergiephysik*, pages 57–111. Springer Berlin Heidelberg, Berlin, Heidelberg, 2017.

[Dur08]   J. Durst. *Modellierung und Simulation physikalischer Eigenschaften photonenzaehlender Roentgenpixeldetektoren fuer die Bildgebung*. PhD thesis, Erlangen Center for Astroparticle Physics, 2008.

[Fan47]   U. Fano. Ionization Yield of Radiations. II. the Fluctuations of the Number of Ions. *Phys. Rev.*, 72:26–29, Jul 1947.

[FCG+15]   E. Frojdh, M. Campbell, M. De Gaspari, S. Kulis, X. Llopart, T. Poikela, and L. Tlustos. Timepix3: first measurements and characterization of a hybrid-pixel detector working in event driven mode. *Journal of Instrumentation*, 10(01):C01039, 2015.

[GBG+16]   St. Gohl, B. Bergmann, C. Granja, A. Owens, M. Pichotka, S. Polansky, and S. Pospisil. Measurement of particle directions in low earth orbit with a Timepix. *Journal of Instrumentation*, 11(11):C11023, 2016.

[Geo15]   S. P. George. *Dosimetric Applications of Hybrid Active Pixel Detectors*. PhD thesis, School of Physics Faculty of Engineering and Information Science, University of Wollongong, 12 2015.

[Gla52]   D. A. Glaser. Some Effects of Ionizing Radiation on the Formation of Bubbles in Liquids. *Phys. Rev.*, 87:665–665, Aug 1952.

[GLRS87]   E. Gatti, A. Longoni, P. Rehak, and M. Sampietro. Dynamics of Electrons in Drift Detectors. *Nuclear Instruments and Methods in Physics Research A*, 253:393–399, 1987.

[GM28]   H. Geiger and W. Müller. Elektronenzählrohr zur Messung schwächster Aktivitäten. *Naturwissenschaften*, 16(31):617–618, Aug 1928.

[GPV+16]   C. Granja, S. Polansky, Z. Vykydal, S. Pospisil, A. Owens, Z. Kozacek, K. Mellab, and M. Simcak. The SATRAM Timepix spacecraft payload in open space on board the Proba-V satellite for wide range radiation monitoring in LEO orbit. *Planetary and Space Science*, 125(Supplement C):114 – 129, 2016.

[HHJ+08]   T. Holy, E. Heijne, J. Jakubek, S. Pospisil, J. Uher, and Z. Vykydal. Pattern recognition of tracks induced by individual quanta of ionizing radiation in Medipix2 silicon detector. *Nuclear Instruments and Methods in Physics Research Section A: Accelerators, Spectrometers, Detectors and Associated Equipment*, 591(1):287 – 290, 2008. Radiation Imaging Detectors 2007: Proceedings of the 9th International Workshop on Radiation Imaging Detectors.

[HK91]   M. M. Hindi and R. L. Kozub. Double K-shell vacancy production in the electron capture decay of ^{139}Ce. *Phys. Rev. C*, 43:461–469, Feb 1991.

[HLR+97]   L. A. Hamel, L. Lessard, L. Rainville, V. Zacek, and B. Sur. A Superheated droplet detector for dark matter search. *Nucl. Instrum. Meth.*, A388:91–99, 1997.

[HOvdB14] C. C. T. Hansson, A. Owens, and J. v. d. Biezen. X-ray, γ-ray and neutron detector development for future space instrumentation. *Acta Astronautica*, 93(Supplement C):121 – 128, 2014.

[HVP+14]   S. Hoang, R. Vilalta, L. Pinsky, M. Kroupa, N. Stoffle, and J. Idarraga. Data analysis of tracks of heavy ion particles in timepix detector. *Journal of Physics: Conference Series*, 523(1):012026, 2014.

[HWK03]   M. M. Hindi, C. A. White, and R. L. Kozub. Double K-shell ionization probability in ^{54}Mn. *Phys. Rev. C*, 68:014306, Jul 2003.

[Jak09]   J. Jakubek. Semiconductor pixel detectors and their applications in life sciences. *Journal of Instrumentation*, 4(03):P03013, 2009.

[Jak11]   J. Jakubek. Precise energy calibration of pixel detector working in time-over-threshold mode. *Nuclear Instruments and Methods in Physics Research Section A: Accelerators, Spectrometers, Detectors and Associated Equipment*, 633, Supplement 1:S262 – S266, 2011. 11th International Workshop on Radiation Imaging Detectors (IWORID).

[JCH+08]   J. Jakubek, A. Cejnarova, T. Holy, S. Pospisil, J. Uher, and Z. Vykydal. Pixel detectors for imaging with heavy charged particles. *Nuclear Instruments and Methods in Physics Research Section A: Accelerators, Spectrometers, Detectors and Associated Equipment*, 591(1):155 – 158, 2008. Radiation Imaging Detectors 2007.

[JGH+11]   J. Jakubek, C. Granja, B. Hartmann, O. Jaekel, M. Martisikova, L. Opalka, and S. Pospisil. Selective detection of secondary particles and neutrons produced in ion beam therapy with 3D sensitive voxel detector. *Journal of Instrumentation*, 6(12):C12010, 2011.

[JT]   J. Jakubek and L. Tlustos. Private communication.

[KBC02]   M. Kavcic, M. Budnar, and J. L. Campbell. A database for {KL} ionization satellites in {PIXE}. *Nuclear Instruments and Methods in Physics Research Section B: Beam Interactions with Materials and Atoms*, 196(1–2):16 – 24, 2002.

[KCM13]   P. Kandlakunta, L. R. Cao, and P. Mulligan. Measurement of internal conversion electrons from Gd neutron capture. *Nuclear Instruments and Methods in Physics Research Section A: Accelerators, Spectrometers, Detectors and Associated Equipment*, 705:36 – 41, 2013.

62

[KEE+10] R. T. Kouzes, J. H. Ely, L. E. Erikson, W. J. Kernan, A. T. Lintereur, E. R. Siciliano, D. L. Stephens, D. C. Stromswold, R. M. Van Ginhoven, and M. L. Woodring. Neutron detection alternatives to 3He for national security applications. *Nuclear Instruments and Methods in Physics Research Section A: Accelerators, Spectrometers, Detectors and Associated Equipment*, 623(3):1035 – 1045, 2010.

[KHJ+11] V. Kraus, M. Holik, J. Jakubek, M. Kroupa, P. Soukup, and Z. Vykydal. FITPix - fast interface for Timepix pixel detectors. *Journal of Instrumentation*, 6(01):C01079, 2011.

[KN29] O. Klein and Y. Nishina. Über die Streuung von Strahlung durch freie Elektronen nach der neuen relativistischen Quantendynamik von Dirac. *Zeitschrift für Physik*, 52(11):853–868, Nov 1929.

[Kno89] G. F. Knoll. *Radiation Detection and Measurement; 2nd ed.* Wiley, New York, NY, 1989.

[Kor07] A. Korn. *Spektrale und bildgebende Eigenschaften photonenzählender Röntgendetektoren am Beispiel des Medipix Detektors.* PhD thesis, Friedrich-Alexander-Universität Erlagen-Nürnberg, 2007.

[Kre06] B. Kreisler. Influenzierte Signale in pixelierten Halbleiter-Röntgen-Detektoren. Master's thesis, Physikalisches Institut der Friedrich-Alexander-Universität Erlangen-Nürnberg, 2006.

[Lan44] L. Landau. On the energy loss of fast particles by ionization. *J. Phys.(USSR)*, 8:201–205, 1944.

[LBCT07] X. Llopart, R. Ballabriga, M. Campbell, and L. Tlustos. Timepix, a 65k programmable pixel readout chip for arrival time, energy and/or photon counting measurements. *Nuclear Instruments and Methods in Physics Research Section A: Accelerators, Spectrometers, Detectors and Associated Equipment*, 581(1-2):485 – 494, 2007. VCI 2007: Proceedings of the 11th International Vienna Conference on Instrumentation .

[Lin03] G. Lindström. Radiation damage in silicon detectors. *Nuclear Instruments and Methods in Physics Research Section A: Accelerators, Spectrometers, Detectors and Associated Equipment*, 512(1 – 2):30 – 43, 2003. Proceedings of the 9th European Symposium on Semiconductor Detectors: New Developments on Radiation Detectors.

[LJZ+14] K. J. Loo, J. Jakubek, J. Zemlicka, M. Petasecca, M. Safavi-Naeini, J. Bucci, M. Zaider, and A.B. Rosenfeld. BrachyView: Feasibility study into the application of Timepix detectors for soft tissue thickness imaging in prostate brachytherapy treatment. *Radiation Measurements*, 71(Supplement C):329 – 332, 2014. Proceedings of the 17th Solid State Dosimetry Conference (SSD17).

[LNST63] J. Lindhard, V. Nielsen, M. Scharff, and P. V. Thomsen. *Integral equations governing radiation effects.* Munksgaard i komm., 1963.

[LR07] C. Leroy and P.-G. Rancoita. Particle interaction and displacement damage in silicon devices operated in radiation environments. *Reports on Progress in Physics*, 70(4):493, 2007.

[LS06] P. W. Lisowski and K. F. Schoenberg. The Los Alamos Neutron Science Center. *Nuclear Instruments and Methods in Physics Research Section A: Accelerators, Spectrometers, Detectors and Associated Equipment*, 562(2):910 – 914, 2006. Proceedings of

the 7th International Conference on Accelerator Applications (AccApp05) 7th International Conference on Accelerator Applications.

[MG81]   L. C. Maximon and H. A. Gimm. Pair production in the field of atomic electrons. *Phys. Rev. A*, 23:172–185, January 1981.

[MJG⁺11]   M. Martisikova, J. Jakubek, C. Granja, B. Hartmann, L. Opalka, S. Pospisil, and O. Jäkel. Measurement of secondary radiation during ion beam therapy with the pixel detector Timepix. *Journal of Instrumentation*, 6(11):C11014, 2011.

[Mol99]   M. Moll. *Radiation Damage in Silicon Particle Detectors.* PhD thesis, University of Hamburg, 1999.

[MPX]   Medipix Collaboration. `http://medipix.web.cern.ch/`. Accessed on 30.10.2017.

[MSBN08]   D. Mitra, M. Sarkar, D. Bhattacharya, and L. Natarajan. Satellites, hypersatellites and RAE from Ti, V, Cr, Mn and Fe in photoionisation. *X-Ray Spectrometry*, 37(6):585–594, 2008.

[nie]   NIEL Calculator. `http://www.sr-niel.org/index.php/niel-calculator`. Accessed on 30.10.2017.

[NS83]   H. J. Nagy and G. Schupp. Double K-shell ionization in the electron capture decays of ^{65}Zn. *Phys. Rev. C*, 27:2887–2892, Jun 1983.

[ntd]   Nuclear Track Detectors. `http://www.iaea.org/inis/collection/NCLCollectionStore/_Public/25/019/25019093.pdf`. Accessed on 30.10.2017.

[O⁺14]   K. A. Olive et al. Review of particle physics. *Chin. Phys.*, C38:090001, 2014.

[Owe12]   A. Owens. *Compound Semiconductor Radiation Detectors.* CRC Press, Taylor & Francis Group, 6000 Broken Sound Parkway NW, Suite 300, 2012.

[PANJ09]   A. Perez-Andujar, W. D. Newhauser, and P. M. DeLuca Jr. Neutron production from beam-modifying devices in a modern double scattering proton therapy beam delivery system. *Physics in Medicine & Biology*, 54(4):993, 2009.

[PBJ⁺08]   M. Platkevic, V. Bocarov, J. Jakubek, S. Pospisil, V. Tichy, and Z. Vykydal. Signal processor controlled USB2.0 interface for Medipix2 detector. *Nuclear Instruments and Methods in Physics Research Section A: Accelerators, Spectrometers, Detectors and Associated Equipment*, 591(1):245 – 247, 2008. Radiation Imaging Detectors 2007.

[PC63]   J. G. Pengra and B. Crasemann. Energy Spectrum of Atomic Electrons Ejected in Electron-Capture Decay of Fe^{55}. *Phys. Rev.*, 131:2642–2648, Sep 1963.

[PEG⁺11]   L. S. Pinsky, A. Empl, A. Gutierrez, J. Jakubek, H. Kitamura, J. Miller, C. Leroy, N. Stoffle, S. Pospisil, Y. Uchihori, N. Yasuda, and C. Zeitlin. Penetrating heavy ion charge and velocity discrimination with a TimePix-based Si detector (for space radiation applications). *Nuclear Instruments and Methods in Physics Research Section A: Accelerators, Spectrometers, Detectors and Associated Equipment*, 633(Supplement 1):S190 – S193, 2011. 11th International Workshop on Radiation Imaging Detectors (IWORID).

[Peu00]   A. J. Peurrung. Recent developments in neutron detection. *Nuclear Instruments and Methods in Physics Research Section A: Accelerators, Spectrometers, Detectors and Associated Equipment*, 443(2):400 – 415, 2000.

[Pin17]   Pinfold, J. The MoEDAL experiment at the LHC. *EPJ Web Conf.*, 145:12002, 2017.

[PLSN+13] M. Petasecca, K. J. Loo, M. Safavi-Naeini, Z. Han, P. E. Metcalfe, S. Meikle, S. Pospisil, J. Jakubek, J. A. Bucci, M. Zaider, M. L. F. Lerch, Y. Qi, and A. B. Rosenfeld. BrachyView: Proof-of-principle of a novel in-body gamma camera for low dose-rate prostate brachytherapy. *Medical Physics*, 40(4):041709–n/a, 2013. 041709.

[PMC+13]   A. Pietropaolo, F. Murtas, G. Claps, L. Quintieri, D. Raspino, G. Celentano, A. Vannozzi, and O. Frasciello. A new 3He-free thermal neutrons detector concept based on the GEM technology. *Nuclear Instruments and Methods in Physics Research Section A: Accelerators, Spectrometers, Detectors and Associated Equipment*, 729:117 – 126, 2013.

[PP53]   H. Primakoff and F. T. Porter. Atomic Excitation and Ionization Accompanying Orbital Electron Capture by Nuclei. *Phys. Rev.*, 89:930–937, Mar 1953.

[PPW+14]   T. Poikela, J. Plosila, T. Westerlund, M. Campbell, M. De Gaspari, X. Llopart, V. Gromov, R. Kluit, M. van Beuzekom, F. Zappon, V. Zivkovic, C. Brezina, K. Desch, Y. Fu, and A. Kruth. Timepix3: a 65K channel hybrid pixel readout chip with simultaneous ToA/ToT and sparse readout. *Journal of Instrumentation*, 9(05):C05013, 2014.

[PSE+11]   L. Pinsky, N. Stoffle, A. Empl, J. Jakubek, S. Pospisil, C. Leroy, H. Kitamura, N. Yasuda, and Y. Uchihori. Application of the Medipix2 technology to space radiation dosimetry and hadron therapy beam monitoring. *Radiation Measurements*, 46(12):1610 – 1614, 2011. Proceedings of the 16th Solid State Dosimetry Conference , September 19-24 , Sydney , Australia.

[Ram39]   S. Ramo. Currents induced by Electron Motion. In *Proceedings of the I.R.E*, volume 27, pages 584–585, Sept. 1939.

[RG08]   E. Rutherford and H. Geiger. An Electrical Method of Counting the Number of α-Particles from Radio-Active Substances. *Proceedings of the Royal Society of London. Series A, Containing Papers of a Mathematical and Physical Character*, 81(546):141–161, 1908.

[RJKcv+13] G. Rusev, M. Jandel, M. Krtička, C. W. Arnold, T. A. Bredeweg, A. Couture, W. A. Moody, S. M. Mosby, and J. L. Ullmann. Cascade γ rays following capture of thermal neutrons on ^{113}Cd. *Phys. Rev. C*, 88:057602, Nov 2013.

[Ros52]   B. Rossi. *High Energy Particles*. Prentice Hall, Englewood Cliffs, NJ, 1952.

[RT74]   M. T. Robinson and I. M. Torrens. Computer simulation of atomic-displacement cascades in solids in the binary-collision approximation. *Phys. Rev. B*, 9:5008–5024, Jun 1974.

[SAA+15]   A. Sopczak, B. Ali, N. Asbah, B. Bergmann, K. Bekhouche, D. Caforio, M. Campbell, E. Heijne, C. Leroy, A. Lipniacka, M. Nessi, S. Pospisil, F. Seifert, J. Solc, P. Soueid, M. Suk, D. Turecek, and Z. Vykydal. MPX Detectors as LHC Luminosity Monitor. *Nuclear Science, IEEE Transactions on*, 62(6):3225–3241, Dec 2015.

[Sat65]   A. R. Sattler. Ionization Produced by Energetic Silicon Atoms within a Silicon Lattice. *Phys. Rev.*, 138:A1815–A1821, Jun 1965.

[SH85]   H. G. Spieler and E. E. Haller. Assessment of Present and Future Large-Scale Semiconductor Detector Systems. *IEEE Transactions on Nuclear Science*, 32(1):419–426, Feb 1985.

[Sho38]   W. Shockley. Currents to conductors induced by a moving point charge. *Journal of Applied Physics*, 9(10):635–636, 1938.

[SJSF06]   A. Surzhykov, U. D. Jentschura, T. Stöhlker, and S. Fritzsche. Radiative electron capture into high-Z few-electron ions: Alignment of the excited ionic states. *Phys. Rev. A*, 73:032716, Mar 2006.

[SMM03]   J. R. Srour, C. J. Marshall, and P. W. Marshall. Review of displacement damage effects in silicon devices. *IEEE Transactions on Nuclear Science*, 50(3):653–670, June 2003.

[SPK⁺15]   N. Stoffle, L. Pinsky, M. Kroupa, S. Hoang, J. Idarraga, C. Amberboy, R. Rios, J. Hauss, J. Keller, A. Bahadori, E. Semones, D. Turecek, J. Jakubek, Z. Vykydal, and S. Pospisil. Timepix-based radiation environment monitor measurements aboard the International Space Station. *Nuclear Instruments and Methods in Physics Research Section A: Accelerators, Spectrometers, Detectors and Associated Equipment*, 782(Supplement C):143 – 148, 2015.

[sri]   SRIM: The Stopping and Range of Ions in Matter. `http://www.srim.org/`. Accessed on 30.10.2017.

[THJ⁺11]   D. Turecek, T. Holy, J. Jakubek, S. Pospisil, and Z. Vykydal. Pixelman: a multiplatform data acquisition and processing software package for Medipix2, Timepix and Medipix3 detectors. *Journal of Instrumentation*, 6(01):C01046, 2011.

[TJS16]   D. Turecek, J. Jakubek, and P. Soukup. USB 3.0 readout and time-walk correction method for Timepix3 detector. *Journal of Instrumentation*, 11(12):C12065, 2016.

[TPJ⁺11a]   D. Turecek, L. Pinsky, J. Jakubek, Z. Vykydal, N. Stoffle, and S. Pospisil. Small Dosimeter based on Timepix device for International Space Station. *Journal of Instrumentation*, 6(12):C12037, 2011.

[TPJ⁺11b]   D. Turecek, L. Pinsky, J. Jakubek, Z. Vykydal, N. Stoffle, and S. Pospisil. Small Dosimeter based on Timepix device for International Space Station. *Journal of Instrumentation*, 6(12):C12037, 2011.

[vdHVvB⁺17] B. van der Heijden, J. Visser, M. van Beuzekom, H. Boterenbrood, S. Kulis, B. Munneke, and F. Schreuder. SPIDR, a general-purpose readout system for pixel ASICs. *Journal of Instrumentation*, 12(02):C02040, 2017.

[VJHP06]   Z. Vykydal, J. Jakubek, T. Holy, and S. Pospisil. A Portable Pixel Detector Operating as an Active Nuclear Emulsion and Its Application for X-ray and Neutron Tomography. In Michele Barone, Emilio Borchi, Andrea Gaddi, Claude Leroy, Larry Price, Pier-Giorgio Rancoita, and Randal Ruchti, editors, *Proceedings of the 9th Conference, Villa Olmo, Como*, pages 779–784. World Scientific Publishing, 2006.

[Wil11]   C. T. R. Wilson. On a Method of Making Visible the Paths of Ionising Particles through a Gas. *Proceedings of the Royal Society of London. Series A, Containing Papers of a Mathematical and Physical Character*, 85(578):285–288, 1911.

List of publications

Peer reviewed articles:

- **B. Bergmann**, P. Burian, P. Manek, S. Pospisil, *"3D reconstruction of particle tracks in a 2 mm thick CdTe hybrid pixel detector"*, accepted for publication in the **European Physical Journal C**, 2019.

- X. Wu, G. Ambrosi, P. Azzarello, **B. Bergmann**, B. Bertolucci, F. Cadoux, M. Campbell, M. Kole, S. Krucker, G. Maehlum, D. Meier, M. Paniccia, L. Pinsky, C. Plainaki, S. Pospisil, T. Stein, P.A. Thonet, A. Tykhonov, *"Penetrating Particle ANalyzer"*, accepted for publication in **Advances in Space Research**, 2019.

- P. Burian, P. Broulim, **B. Bergmann**, *"Study of Power Consumption of Timepix3 Detector"*, **JINST 14** C01001, 2019.

- St. Gohl, **B. Bergmann**, H. Evans, P. Nieminen, A. Owens, S. Pospisil, *"Study of the radiation fields in LEO with the Space Application of Timepix Radiation Monitor (SATRAM)"*, **Advances in Space Research**, Vol. **63**, Issue 1, Pages 1646-1660, 2019.

- P. Burian, P. Broulim, **B. Bergmann**, V. Georgiev, S. Pospisil, L. Pusman, J. Zich, *"Timepix3 detector network at ATLAS experiment"*, **JINST 13** C11024, 2018.

- T. Gao, C. da Via, **B. Bergmann**, P. Burian, S. Pospisil, *"Characterization of Timepix3 with 3D sensor"*, **JINST 13** C12021, 2018.

- P. Rubovic, D. Ekendahl, Z. Vykydal, J. Hulka, **B. Bergmann**, S. Pospisil, I. Stekl, *"Dosimetry in mixed neutron-gamma fields with a Timepix detector"*, **Radiation Measurements**, Volume **119**, Pages 22-26, ISSN 1350-4487, 2018.

- A. Sopczak, B. Ali, J. Begera, **B. Bergmann**, T. Billoud, B. Biskup, P. Burian, D. Caforio, E. Heijne, J. Janecek, C. Leroy, P. Manek, Y. Mora, S. Pospisil, M. Suk, Z. Svoboda, *"Precision Measurements of Induced Radioactivity and Absolute Luminosity Determination With TPX Detectors in LHC Proton-Proton Collisions at 13 TeV"*, **IEEE Trans. Nucl. Sc.**, Vol. **65**, No. 7, 2018.

- A. Sopczak, B. Ali, J. Begera, **B. Bergmann**, T. Billoud, B. Biskup, P. Burian, D. Caforio, E. Heijne, J. Janecek, C. Leroy, P. Manek, Y. Mora, S. Pospisil, T. Seidler, M. Suk, Z. Svoboda, *"Determination of Luminosity With Thermal Neutron Counting Using TPX Detectors in the ATLAS Cavern in LHC Proton-Proton Collisions at 13 TeV"*, **Trans. Nucl. Sc.**, Vol. **65**, No. 7, 2018.

- P. Smolyanskiy, **B. Bergmann**, G. Chelkov, S. Kotov, U. Kruchonak, D. Kozhevnikov, Y. Mora Sierra, I. Stekl, and A. Zhemchugov, *"Properties of GaAs:Cr-based Timepix detectors"*, **JINST 13** T02005, 2018.

- P. Burian, P. Broulim, V. Georgiev, **B. Bergmann**, and S. Pospisil, *"Particle telescope with Timepix3 pixel detectors"*, **JINST 13** C01002, 2017.

- P. Burian, P. Broulim, M. Jara, V. Georgiev, and **B. Bergmann**, *"Kathrine: Ethernet Embedded Readout Interface for Timepix3"*, **JINST 12** C11001, 2017.

- P. Rubovic, **B. Bergmann**, D. Eckendahl, J. Hulka, L. Judas, Z. Kohout, S. Pospisil, I. Stekl, *"Timepix detector as a tool for x-ray and gamma dosimetry"*, **Radiation Measurements**, Vol. **107**, 39-24, 2017.

- A. Sopczak, B. Ali, T. Asawatavonvanich, J. Begera, **B. Bergmann**, T. Billoud, P. Burian, I. Caicedo, D. Caforio, E. Heijne, J. Janecek, C. Leroy, P. Manek, K. Mochizuki, Y. Mora, J. Pacik, C. Papadatos, M. Platkevic, S. Polansky, S. Pospisil, M. Suk, Z. Svoboda, *"Precision Luminosity of LHC Proton-Proton Collisions at 13 TeV Using Hit-Counting with TPX Pixel Devices"*, **IEEE Trans. Nucl. Sc.**, Vol. **64**, No. 3, 2017.

- **B. Bergmann**, M. Pichotka, S. Pospisil, J. Vycpalek, P. Burian, P. Broulim, and J. Jakubek, *"3D track reconstruction capability of a silicon hybrid active pixel detector"*, **European Physical Journal C**, Vol. **77**, 2017.

- **B. Bergmann**, I. Caicedo, C. Leroy, S. Pospisil, and Z. Vykydal, *"ATLAS-TPX: A two-layer pixel detector setup for neutron detection and radiation field characterization"*, **JINST 11** P10002, 2016

- **B. Bergmann**, S. Pospisil, I. Caicedo, J. Kierstead, H. Takai, E. Frojdh, *"Ionizing Energy Depositions After Fast Neutron Interactions in Silicon"*, **IEEE Trans. Nucl. Sc.**, Vol. **63**, No. 4, 2016

- **B. Bergmann**, T. Michel, A. Surzhykov, and S. Fritzsche, *"Angular correlation function of the hypersatellite-satellite x-ray cascade following K-shell electron capture of 55-Fe"*, **Phys. Rev. C 94**, 014611, 2016.

- St. Gohl, **B. Bergmann**, C. Granja, A. Owens, M. Pichotka, S. Polansky, and S. Pospisil, *"Measurement of particle directions in low earth orbit"*, **JINST 11** C11023, 2016.

- A. Sopczak, B. Ali, N. Asbah, **B. Bergmann**, K. Bekhouche, D. Caforio, M. Campbell, E. Heijne, C. Leroy, A. Lipniacka, M. Nessi, S. Pospisil, F. Seifert, J. Solc, P. Soueid, M. Suk, D. Turecek, and Z. Vykydal, *"MPX Detectors as LHC Luminosity Monitor"*, **IEEE Trans. Nucl. Sc.**, Vol. **62**, No. 6, pp.3225-3241, 2015.

- T. Michel, **B. Bergmann**, J. Durst, M. Filipenko, T. Gleixner, and K. Zuber, *"Measurement of the double K-shell vacancy creation probability in the electron-capture decay of 55-Fe with active pixel detectors"*, **Phys. Rev. C 89**, 014609, 2014.

- **B. Bergmann**, R.O. Nelson, J.M. O'Donnell, S. Pospisil, J. Solc, H. Takai, Z. Vykydal, *"Time-of-Flight Measurement of Fast Neutrons with Timepix Detectors"*, **JINST 9** C05048, 2014.

Non peer reviewed articles:

- St. Gohl, **B. Bergmann**, S. Pospisil, *"Study of a new miniaturized radiation monitor based on previous experience with the Space Application of the Timepix Radiation Monitor (SATRAM)"*, 2018 IEEE Nuclear Science Symposium and Medical Imaging Conference (NSS/MIC), 2018.

- P. Manek, J. Begera, **B. Bergmann**, P. Burian, J. Janecek, S. Polansky, S. Pospisil, and M. Suk, *"Software system for data acquisition and analysis operating the ATLAS-TPX network"*, IEEE 22nd International Conference on Applied Electronics, Czech Republic, 2017.

- I. Caicedo, **B. Bergmann**, M. Kralik, V. Kraus, C. Leroy, S. Pospisil, M. Suk, Z. Vykydal, *"Characterization of a Timepix detector-based hodoscope for the measurement of mixed radiation field"*, 2014 IEEE Nuclear Science Symposium and Medical Imaging Conference (NSS/MIC), 2014.

Acknowledgements

As it is common practice, I would also like to use the space at the end of the thesis to thank the people, who have been supporting and inspiring me - not only but mainly - in the sometimes hard life in research (when waiting for the beam, when performing actual measurements, when evaluating the data, when being at conferences, when writing publications, reports and proposals, ...). Most of them were also helping me to find a way in a foreign country with a not-very-easy-to-learn-and-understand language. It is a country which has become more than a second home for me.

And special thanks go to ...

- **Gisela Anton** for accepting me as a PhD student.

- **Thilo Michel** for believing in the hypersatellite measurement(s), the patience with it and his demand for perfection. Even if it took quite some time, the results were worth the effort.

- **Stanislav Pospisil**, whom I cannot thank enough for always being available for discussions (even Fridays from 10 pm to midnight), for encouraging me to do measurements, to attend and present my results at conferences, for sharing with me his passion for physics and pixel detectors (Timepix in particular), and much more.

- **Ivan Stekl** for pushing me to finish the thesis and giving me all the freedom I needed to do so.

- **Claude Leroy** for always being available to read through my papers before submission, his valuable feedback, and for his advice in private discussions.

- **Zdenek Vykydal** for all the help when I was new to the Czech Republic, for helping me finding a flat, showing me how to do the administrative stuff in IEAP, and for the nice times on business trips (Los Alamos, Geneva, Vienna, ...).

- All secretaries, I have bothered (sometimes maybe too much) with the accounting of business trips and other (more or less) important paperwork: **Sona Stichova, Martina Vanisova, Dana Machynkova, Elena Ryparova, Tereza Vykadalova, and Marie Popova** (random order).

- The cool guys: M.Tc. (Master of Timepix calibrations) **Ivan Caicedo** and **Kevin Loo** for the discussions during lunch, hanging out, invitations to all kinds of parties, sharing room(s) on business trips, bringing me food when I was sick. Another big thanks to Kevin for reading, finding and correcting my English mistakes in the ARDENT reports (there were a few), publications, and finally also in this thesis.

- **Yesid Mora Sierra** for showing me Prague, for always being available to do wire-bonding, for the repair of damaged Timepix assemblies and the charger(s) of my laptop.

- **Petr Burian**, the highly talented electronics and firmware expert, without whom the ATLAS-TPX network would have become a big fail. Thank you for the collaborative work on the Timepix3 readout (Katherine) and the Timepix3 particle telescope. Also, for all more or less valuable discussions (about electronics, physics, life and famous, but already dead, Czech musicians) on our long journeys to CERN and when sitting in SPS, the CERN cafeteria or Charly's pub.

- The colleagues that became friends: **Karla Palma, Thomas Billoud, Martin Pichotka**, and **S(t). Gohl.**

- The students, I had the pleasure to supervise and work with: **Petr Manek, Aakash Ravi, Herbert Waage, Jiri Vycpalek,** and **Lukas Meduna**.

- The **ARDENT fellows**, the ARDENT project leader **Marco Silari** and all other people involved. It was a great pleasure to be part of it.

- Everybody from the **Medipix collaboration**.

Last but not least:

- My whole family (including uncles, aunts and cousins), especially my mother and grandmother, my friends, who were and are always there for me. - *Meiner ganzen Familie (mit Onkeln und Tanten, Cousins und Cousinen) - besonders aber meiner Mutter und Großmutter - meinen Freunden, die immer für mich da waren und sind.*